ORIGINAL RESEARCH ARTICLE

# Understanding the High-Temperature Fatigue Crack Growth from Exceptional Nano-α Phases and {10$\bar{1}$2} Deformation Twins in Hot Deformed Titanium Alloy

XIAOYAN WANG, YUANFEI HAN, XIN SU, SHAOPENG LI, GUANGFA HUANG, JIANWEI MAO, and WEIJIE LU

In this study, the fatigue crack growth rate (FCGR) of Ti-6Al-4V alloy at 723 K was measured by direct current potential drop (DCPD) method, and exceptional nano-α phases and {10$\bar{1}$2} deformation twins were newly found at the crack tip in Ti-6Al-4V alloy. The results showed that nano-α phases have Burgers orientation relationships (OR) $(0001)_\alpha//(110)_\beta$, $[\bar{2}110]_\alpha//[\bar{1}11]_\beta$ with β phases. The terraced-structure interface consisted of $(0\bar{1}10)_\alpha//(1\bar{1}2)_\beta$ and $(10\bar{1}0)_\alpha//(1\bar{1}0)_\beta$. Numerous dislocations accumulated in the β phase and became the diffused channels of O and V atoms. The α stabilizers (O element) diffused into the crystal lattice and β stabilizers (V element) spread out of the crystal lattice which accelerated the nano-α phases nucleation. <a> and <c + a> dislocations piled up at the primary α grain, interface and low angle grain boundaries (LAGBs), and dissociated into twinning dislocations to promote the twin nucleation. Dislocation transformation enabled nano-twins to grow through the primary α/β interface and strain transfer led that deformation twins nucleated in the adjacent primary α grains. With the effects of nano-α phases, LAGBs and twins, the resistance of crack propagation increased and the driving force decreased, and resulted in the low FCGR.

XIAOYAN WANG, XIN SU, SHAOPENG LI, GUANGFA HUANG, and JIANWEI MAO are with the State Key Laboratory of Metal Matrix Composites, School of Material Science and Engineering, Shanghai Jiao Tong University, Shanghai 200240, China. YUANFEI HAN and WEIJIE LU are with the State Key Laboratory of Metal Matrix Composites, School of Material Science and Engineering, Shanghai Jiao Tong University, and also with the Shanghai Key Laboratory of Advanced High Temperature Materials and Precision Forming, Shanghai 200240, China. Contact e-mails: hyuf1@sjtu.edu.cn; luweijie@sjtu.edu.cn.
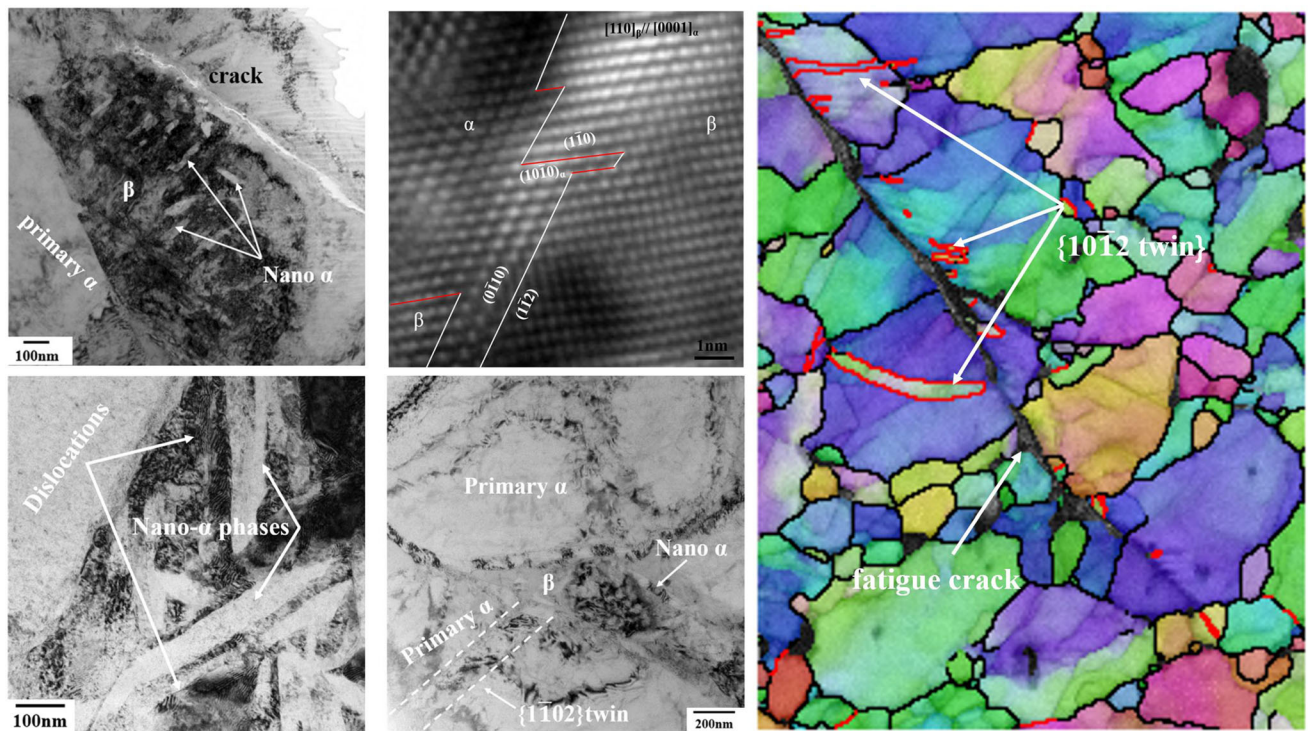
## I. INTRODUCTION

TITANIUM alloys are widely used as structural material, especially in the aerospace due to their high strength and good fatigue properties.[1–3] In the last decades, extensive studies have been carried out to understand the fatigue behavior of Ti-6Al-4V alloy at room temperature. It has been observed that fatigue crack initiated in both primary α grains and lamellar colonies with high Schmid factors (SF) for prismatic slip.[4] Mine et al.[5] reported the fatigue crack growth (FCG) behavior in single-colony lamellar structure of Ti-6Al-4V alloy. The unzipping process by prismatic slip dominated the FCG for the soft colony, while basal slip and non-basal systems contributed to the FCG for the hard colony. Moreover, it has been found that α grains which were well orientated for basal slip, and (0001) twist grain boundaries (GBs) were critical configurations for the dwell-fatigue crack initiation.[6] Except for grain orientation, the microstructure also has significant effect on the FCG behavior. For example, it has been found that the internal fatigue cracks initiated at the primary α GBs in bimodal microstructure, but nucleated at the α/β interfaces in basket-weave microstructure.[7] In addition, strain and stress conditions also play important roles in fatigue behavior. Jha et al.[8] investigated the effect of strain amplitude on low cycle fatigue in Ti-6Al-4V alloy, the formation of sub-grains resulted in the lower friction stress after the cyclic loading at high strain amplitude. With the stress ratio increasing, different crack initiation modes occurred on the fracture surfaces.[9] Above all, the fatigue behavior of Ti-6Al-4V alloy is complicated and sensitive to the multiple factors, including grain orientation, microstructure, strain amplitude, stress ratio, etc.[4–9]

However, titanium alloys are often used in relatively high service temperature, it is necessary to understand the high-temperature fatigue mechanism in detail. Up to now, fewer work has been carried out on the high-temperature fatigue behavior of titanium alloys. Additional factors such as oxides[10] and secondary phases[11] would show special characteristic, and resulted in the great complexity of fatigue behavior. The oxides resulted in crack closure and reduced the FCGR.[10] Moreover, $Ti_3Al$ phases precipitated in Timetal 834 and resulted in strengthening effect.[11] In addition, it has been measured the FCGR of Ti-6Al-4V alloy at high temperature and it was concluded that the transition mechanisms of FCG were closely related to service conditions.[12] However, microstructural evolution would occur nearby the crack tip when the specimens experienced the coupling effect of heat and force. Therefore, in this work, the secondary phases precipitation and the deformation twins nucleation were investigated intensively to understand the high-temperature fatigue behavior of titanium alloys.

The plastic deformation of Ti-6Al-4V alloy is dominated by high fraction of HCP-α phases, but limited slip systems exist in HCP-α phase, including $\{0001\}\langle 11\bar{2}0\rangle$

basal slip, $\{10\bar{1}0\}\langle11\bar{2}0\rangle$ prismatic slip, and pyramidal slip.[13,14] It's difficult to activate pyramidal slip at room temperature, thus, twins are activated to coordinate plastic deformation of c-axis.[15–18] In addition, $\{10\bar{1}2\}$ deformation twin is the dominant type in titanium alloys at room temperature because of its low shear strain.[19,20] Related to the effect of twins on fatigue cracking, Bosh et al.[21] found that the formation of $\{10\bar{1}2\}$ twins affected the cohesive properties of GBs and resulted in its fatigue cracking. However, twin nucleation is difficult for Ti-6Al-4V alloy due to the addition of Al except at high strain rate.[22,23] For instance, Wielewski et al.[23] reported that $\{11\bar{2}1\}$ and $\{10\bar{1}2\}$ deformation twins occurred during the classic Taylor impact test, twins preferentially formed in the macrozones orientated for easy <a>-type slip. The nucleation and propagation of $\{1\bar{1}02\}$ deformation twins occurred near fatigue crack surfaces, the dissociation of basal <a> type dislocations accumulated at $\alpha/\beta$ interface and contributed to the twin nucleation.[24] As well known, the critical resolved shear stress (CRSS) of pyramidal slip decreases rapidly with increasing temperature, thus, it's much easier to activate pyramidal slip but difficult to nucleate deformation twins at high temperature.[25] Although mechanical twinning occurred in severe plastic deformed Ti-6Al-4V alloy at 1073 K,[26] they believed that the occurrence of $\{10\bar{1}1\}$ twins was attributed to the imposed high stress, strain and strain rate during equal channel angular extrusion (ECAE). However, the twin nucleation at high temperature was not been understood fully, so it is very necessary to understand the formation of deformation twins during high-temperature fatigue.

Above all, the fatigued sample was characterized via focused ion beam (FIB)-transmission electron microscopy (TEM), transmission Kikuchi diffraction (TKD), scanning electron microscope (SEM) and electron backscatter diffraction (EBSD). To understand the exceptional phenomenon of secondary $\alpha$ phases and $\{10\bar{1}2\}$ deformation twins in Ti-6Al-4V alloy during high-temperature fatigue, we characterized the interface structure and orientation relationship (OR) between nano-$\alpha$ phases and $\beta$ phases, then established the relationship between the precipitation of nano-$\alpha$ phases and the formation of $\{10\bar{1}2\}$ deformation twins. Finally, we compared the FCGR with previously published work, and concluded that the formation of nano-$\alpha$ phases, $\{10\bar{1}2\}$ deformation twins, and LAGBs reduced the FCGR of Ti-6Al-4V alloy during high temperature fatigue.

## II. MATERIAL AND EXPERIMENTAL PROCEDURE

The material investigated in this work is Ti-6Al-4V alloy (6 wt pct Al, 4 wt pct V). Grade I sponge titanium, aluminum thread (98 pct purity) and master alloys Al-V were selected as raw materials. Ti-6Al-4V ingot was melted three times in a consumable vacuum furnace to guarantee homogeneity, then hot forged with a total reduction of 80 pct, and the forged billets with a dimension of 45mm×45mm×800mm was heat treated at 1073 K for 2 hours followed by air cooling, then obtaining equiaxed microstructure.

FCGR test by DCPD method was carried out at 723 K in the atmospheric air by compact tension (CT) specimen which was consistent with the ASTM E399 standard. Sine wave force was loaded on the CT specimen with a thickness of 12.7 mm. The calculated relationship among stress intensity factor, the force and the crack length can be found in ASTM E399, and the fatigue pre-cracking was stopped ($K_{max}$ = 25 MPa m$^{1/2}$, $R$ = 0.3, $f$ = 1 Hz) until $a/W$ is equal to 0.4 (the initial $a/W$ is equal to 0.39). The FCGR was tested ($K_{max}$ = 25 MPa m$^{1/2}$, $R$ = 0.6, $f$ = 0.5 Hz) until $a/W$ is equal to 0.515. Whole test process was performed at 723 K for 45 hours, and the FCGR is $3.6\times10^{-5}$ mm/cycle. Tensile testing with a strain rate of $10^{-3}$/s at 723 K along the forging extension direction was carried out on tensile equipment (Zwick/Roell Z050, Germany). The gauge section had dimensions of 15 mm×4 mm×2 mm. Fatigue crack tip plastic zone (CTPZ) of CT specimen is under plane strain condition, it can be calculated by $r_p \approx 1/6\pi(\Delta K/\sigma_y)^2$, where $\sigma_y$ is the yield strength,[27] its value is 478 ± 5 MPa, thus, the calculated $r_p$ is approximately 50 $\mu$m.

The microstructures were observed by field scanning electron microscopy (FE-SEM, NanoSEM 230, United States). The samples used for SEM analyses were prepared by mechanical grinding, polishing and then etching with Kroll's solution (10 ml HF + 30 ml HNO$_3$ + 100 ml H$_2$O). The grain size, subgrains, local misorientation, Schmid factor and twins were analyzed by electron backscattering diffraction (EBSD) on the NanoSEM 230 instrument (NanoSEM 230, United states). The samples used for EBSD analyses were mechanically ground, prepolished using a monocrystalline diamond suspension and were polished by Leica EM TIC 3X (Leica, Germany). EBSD with a step size of 0.25 $\mu$m was performed in areas on the crack tip with dimensions of 100 $\mu$m × 200 $\mu$m. The acquired EBSD images were processed using HKL CHANNEL5 software, which identifies twins and the corresponding types of twins by comparing the GB misorientation, axis and angle with the twinning relationships. For example, $\{10\bar{1}2\}$ twins led to an 85 deg ±5 deg rotation of the crystal axes around the $\langle1\bar{2}10\rangle$ direction. TEM sample with an area of 5 $\mu$m × 10 $\mu$m was prepared by FIB using Ultra-high resolution SEM-FIB & TOF-SIMS (GAIA3, Czech Republic) and was characterized by TEM (Tecnai G2 F20 S-TWIN, United States) operating at 200KV. TKD with a step size of 10nm was carried out on the TEM sample via FE-SEM (MIRA3, Czech Republic) which can distinguish the nano-phases and analyze their orientation relationships.

## III. RESULTS AND DISCUSSION

High-temperature fatigue is a complicated process of coupling the heat treatment and mechanical loading, including the effects of ageing and plastic deformation,
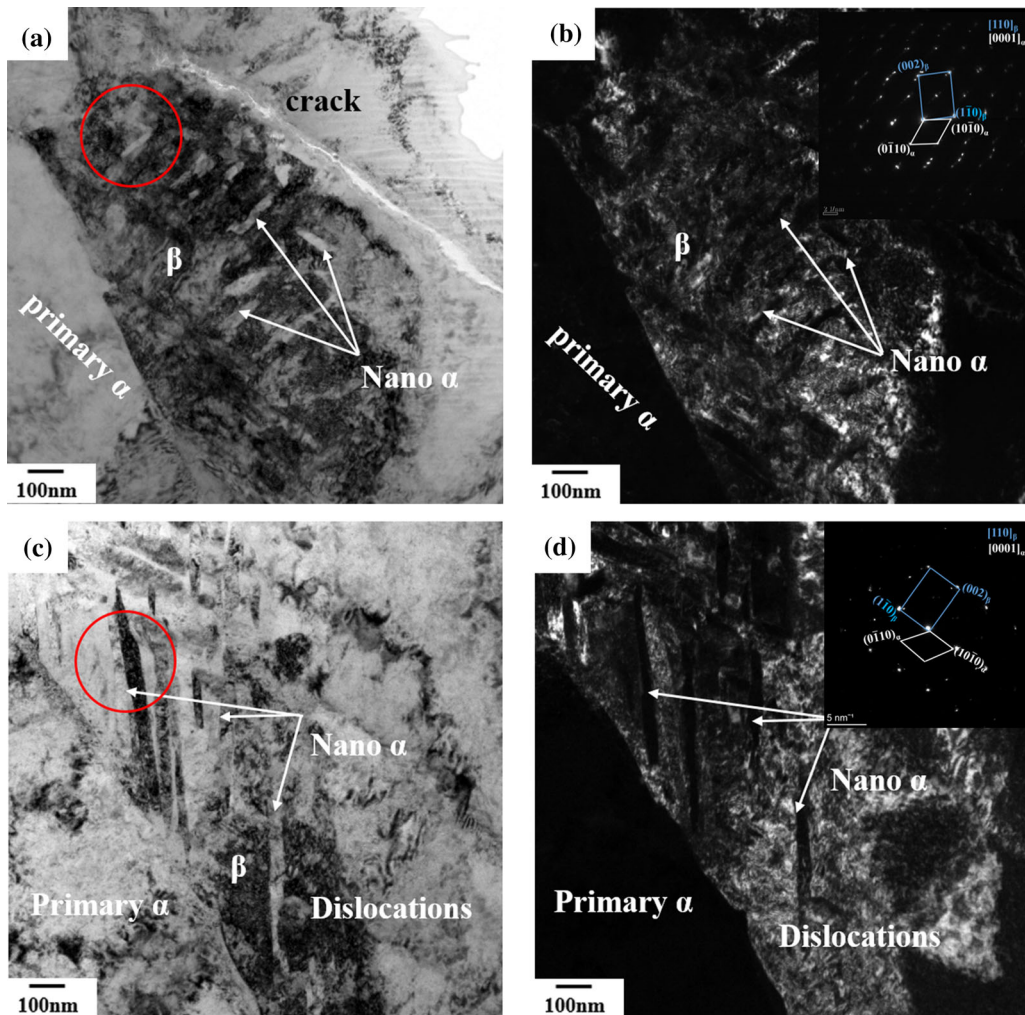
Fig. 1—Nano-α phases precipitate in β phase. (a, c) Bright field (BF) TEM micrographs of nano-α phases; (b, d) Dark field (DF) TEM micrographs of nano-α phases in (a) and (c), respectively.

thus, Ti-6Al-4V alloy should show an exceptional microstructural evolution during the high-temperature fatigue. Element diffusion would occur during the ageing process. Dislocation accumulation would arise at the interface during plastic deformation and stress concentration may result in dislocations decomposing into twinning dislocations. Moreover, dislocations are rapid channels for the atom diffusion, and the interaction between dislocations and element diffusion may result in phase transformation. In this work, the precipitation of nano-phases and the nucleation of deformation twins were discovered at the fatigue crack tip. Figure 1 shows that numerous lenticular nano-α phases precipitate in the β phase near the fatigue crack tip. Obviously, there are numerous dislocation distributing in the β phase while there is low-density dislocation in the nano-α phase. Once the OR between nano-α phase and β phase is not conducive to the dislocations transmission, dislocations jamming would occur at the interface. It is necessary to analyze the OR between nano-α phase and β phase. There are large differences in dislocation density between the primary α and β phases, and the blocking effect of primary α/β interface on the

dislocation slip would bring to severe stress concentration, leading that crack propagates at the interface (Figure 1(a)). Moreover, plenty of dislocations in the β phase accelerate the elements diffusion and facilitate the precipitation of the nano-α phases. To understand the phenomenon of the formation of nano-α phases, the nano-α phases (Figure 1(a)) are selected to analyze the structure of nano-α/β interface and their ORs. These results will be presented in the Section III–A, and the precipitation mechanism will be discussed in detail in the Section III–B.

Figure 2(a) shows that $\{1\bar{1}02\}$ deformation twin nucleates at the α/β interface. Numerous dislocations exist in the grains near the fatigue crack tip. Moreover, interface is a strong obstacle for the dislocation motion. The dislocations at the primary α/β interface may dissociate into the $\{1\bar{1}02\}$ twinning dislocations under the cyclic loading and promote the nucleation of $\{1\bar{1}02\}$ deformation twins. Figure 2(b) shows a high resolution TEM (HRTEM) image of twin/matrix interface. Four main steps are carried out in the HRTEM image to get the atoms of twin/matrix interface (Figure 2(c)): (1)
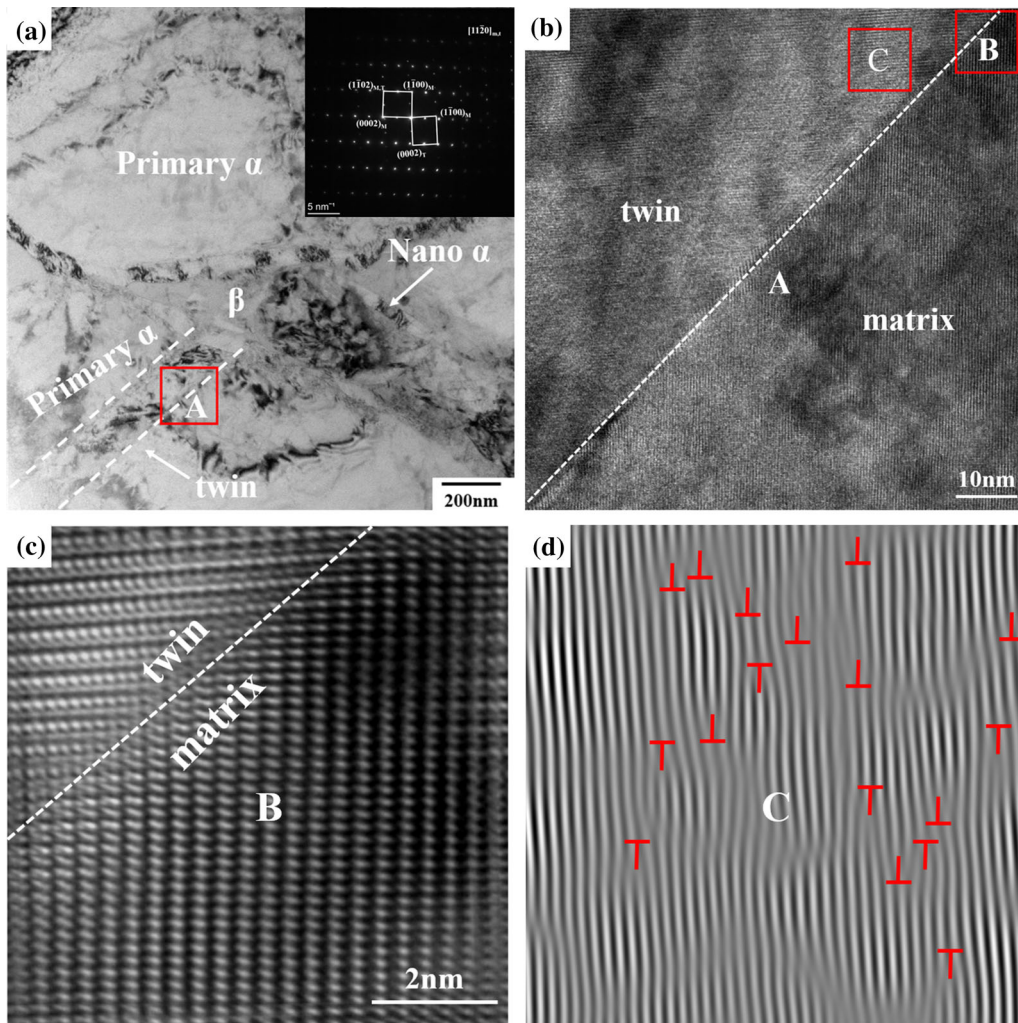
Fig. 2—Deformation twin at the fatigue crack tip region. (*a*) The TEM image of {1$\bar{1}$02} deformation twins; (*b*) The HRTEM image of {1$\bar{1}$02} twin boundary along [11$\bar{2}$0] direction; (*c*) The atoms of twin/matrix interface; (*d*) The IFFT image of dislocations on the prismatic plane of {1$\bar{1}$02} deformation twin.

Select area B; (2) Fast Fourier Transform (FFT); (3) Mask diffraction patterns of twin and matrix and apply mask; (4) Inverse FFT (IFFT). The disordered-atoms arrangement indicates that there are dislocations near the interface and in the twin. Dislocations play important roles in the nucleation and propagation of deformation twins. As shown in Figure 2(d), numerous edge dislocations distribute on the prismatic plane of {1$\bar{1}$02} deformation twin. These dislocations can work as the source of twinning dislocations, and lead to the propagation of deformation twins. The nucleation and propagation of twins will be analyzed in detail in the Section III–C.

## A. The Interfacial Structure and ORs Between Nano-α and β Phases

Figure 3 shows higher magnification TEM images and the structure of nano-α/β interface. A typical nano-grains diffraction pattern proves that nano-α phases exist in β phase. Figure 3(b) shows the relationship between three <a> slips in α phase and three <b> directions in β phase, and most of them are close-packed directions of α-Ti and β-Ti, respectively. It can be found that $[\bar{1}11]_\beta // [\bar{2}110]_\alpha$ and $(110)_\beta // (0001)_\alpha$, these results are consistent with previous work.[24,28] As well know, when β phases transform into α phases, they will have this Burgers OR. Figure 3(c) represents the HRTEM image of nano-α and β structure along $[0001]_\alpha // [110]_\beta$. The nano-α/β interface emerges a terraced structure (Figure 3(d)), which consists of two sets of parallel planes $(0\bar{1}10)_\alpha // (1\bar{1}2)_\beta$ and $(10\bar{1}0)_\alpha // (1\bar{1}0)_\beta$. The interplanar spacings of $(0\bar{1}10)_\alpha$, $(\bar{1}010)_\alpha$, $(1\bar{1}2)_\beta$, and $(1\bar{1}0)_\beta$ are 0.255 nm, 0.255 nm, 0.13 nm and 0.226 nm, respectively. Therefore, the interplanar spacing mismatch between $(10\bar{1}0)_\alpha$ and $(1\bar{1}0)_\beta$ is 12.8 pct which is semi-coherent interface. However, the $(0\bar{1}10)_\alpha // (1\bar{1}2)_\beta$ interface belongs to incoherent interface. Figures 3(e) and (f) show that dislocations are distributed on the $(0\bar{1}10)_\alpha$ and $(\bar{1}010)_\alpha$ planes of nano-α phase near the nano-α/β interface, respectively. Prismatic slip is the first slip system to active in the titanium alloy due to its
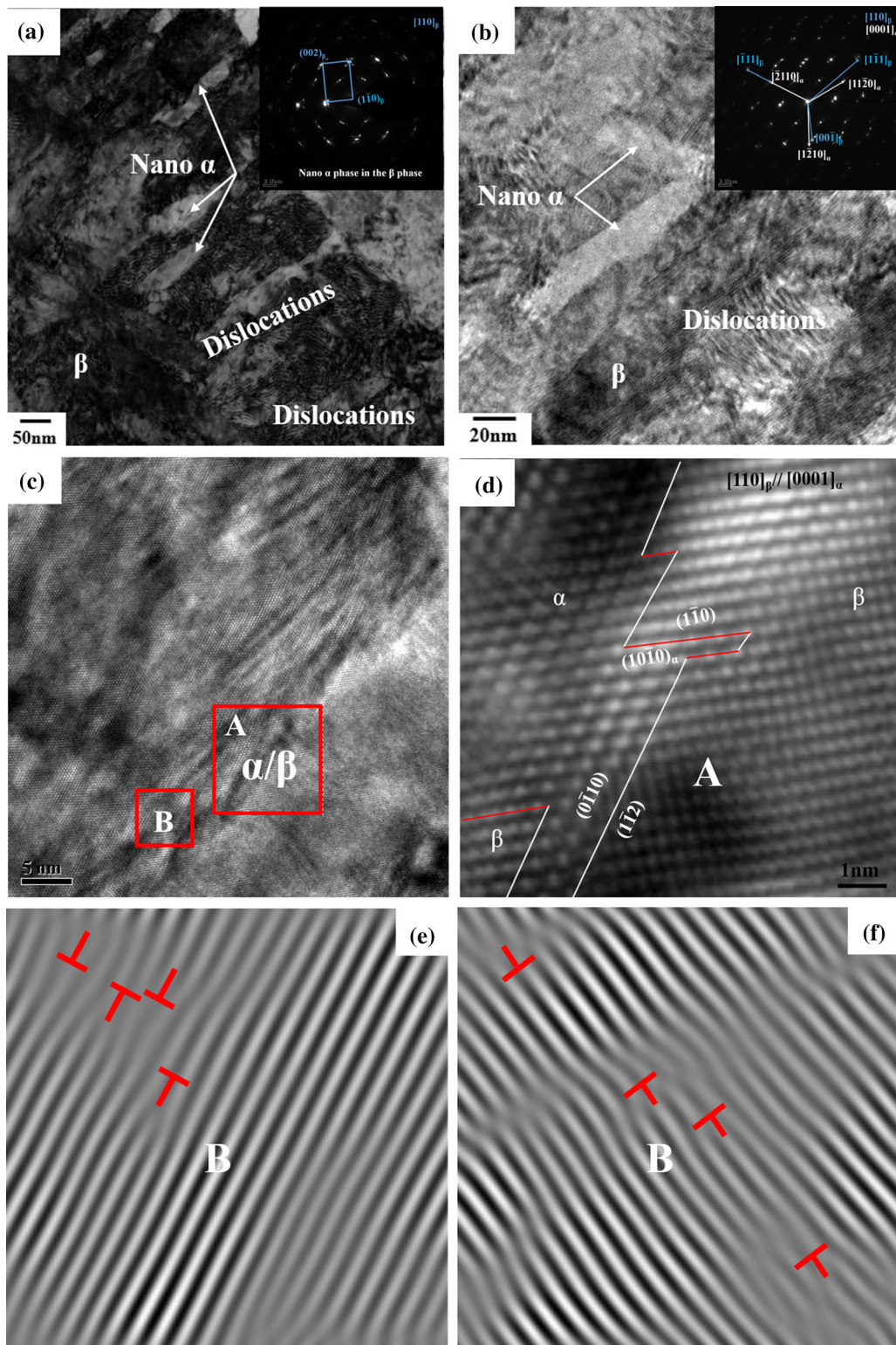
Fig. 3—The nano-α/β interface characterized by TEM. (*a, b*) BF TEM images of nano-α phase in different magnifications; (*c*) HRTEM image of nano-α/β interface; (*d*) The atoms of nano-α/β interface structure along $[0001]_\alpha$//$[\bar{1}10]_\beta$ direction; (*e, f*) IFFT images of dislocations on the prismatic planes of nano-α phase.

lowest CRSS. Owing to the semi-coherent interface/ incoherent interface, numerous edge dislocations pile up near the nano-α/β interface. Moreover, nano-α/β interface works a strong barrier to dislocation slip, once the dislocations sliding directions and slip planes are not conducive to passing through the interface, dislocations would accumulate at the interface and result in stress concentration. In addition, due to the excellent
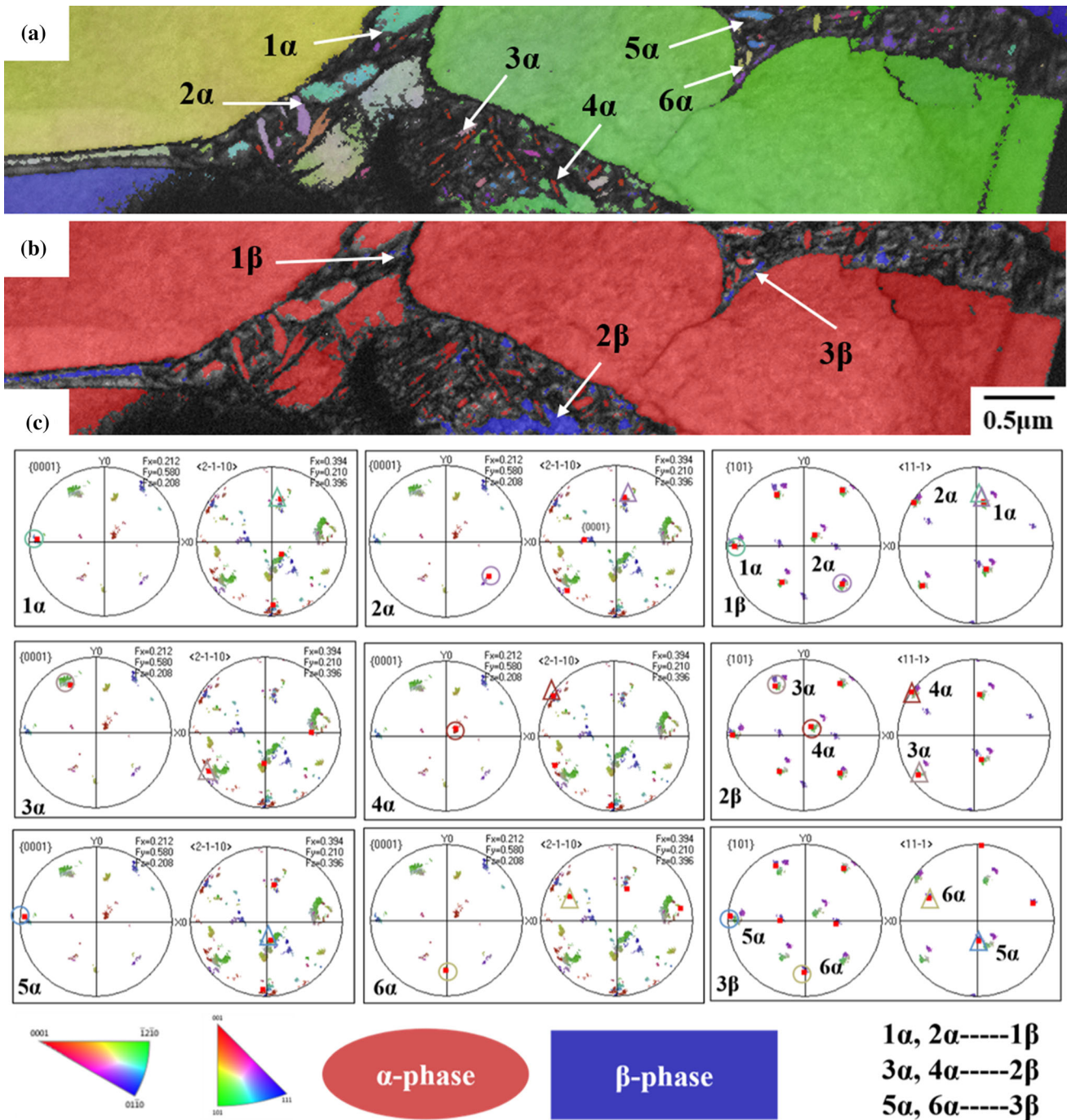
Fig. 4—Nano-$\alpha$ phases precipitate in $\beta$ phase characterized by TKD technology. (*a*) IPF map; (*b*) phase distribution map; (*c*) $\{0001\}_\alpha$, $\{101\}_\beta$, $\langle 2\bar{1}\bar{1}0 \rangle_\alpha$, $\langle 11\bar{1} \rangle_\beta$ pole figures.

deformability of $\beta$ phase, the plenty of slip systems lead to the dislocations pileup in the $\beta$ phase.

Figure 4 shows the crack tip characterized by TKD technology with a smaller step size (10 nm) and higher resolution. The phase distribution diagram (Figure 4b) fully shows that the $\beta$ phases (blue) distribute between the primary $\alpha$ phases (red), and exceptional nano-$\alpha$ phases precipitate in $\beta$ phases. As shown in the inverse pole figure (IPF) map, numerous nano-$\alpha$ phases with different colors show that they precipitate in the $\beta$ phase

with different orientations. Six nano-$\alpha$ grains and three $\beta$ grains are selected to investigate their ORs. As well known, the coincidence of projections in the pole figure indicates that two grains have a parallel relationship. The $\{0001\}_\alpha$, $\{101\}_\beta$, $\langle 2\bar{1}\bar{1}0 \rangle_\alpha$, $\langle 11\bar{1} \rangle_\beta$ pole figures are also shown in Figure 4, circles and triangles (the color is consistent with nano-$\alpha$ grains in the IPF map) mark coincident crystal planes and crystal orientation, respectively. These results show $(0002)_\alpha$ is parallel to one crystal plane of $\{101\}_\beta$, and one crystal direction of
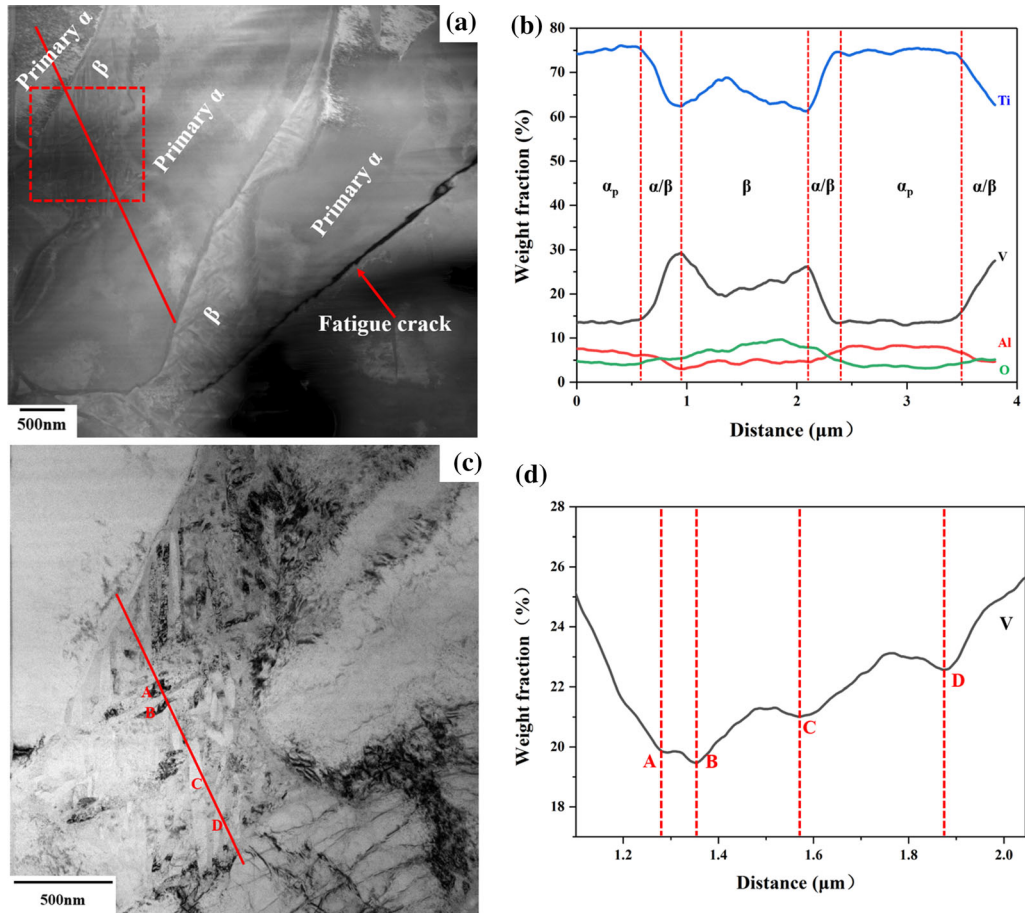
Fig. 5—The distribution of Ti, V, Al and O elements in the primary α phase and β phase. (*a*) The scan area; (*b*) The results of elements distribution; (*c*) Local magnification of nano-α phase in the β phase; (*d*) The result of local V element distribution.

$\langle 2\bar{1}\bar{1}0 \rangle_\alpha$ is parallel to $\langle 11\bar{1} \rangle_\beta$, which are consistent with the TEM results and previous work.[24,28]

### B. *Precipitation Mechanism of Nano-α Phases*

It has been reported some precipitation mechanisms of α phases in β phase: (1) $\beta \rightarrow \beta' \rightarrow \alpha$, which takes place in titanium alloys (rich in β stabilizers). β' phases (bcc structure) are lean in alloy elements and work as the nucleation sites of α phases.[29,30] (2) $\beta \rightarrow w \rightarrow \alpha$, which occurs in titanium alloys (lean in alloy elements) when ageing at low temperature,[31,32] w phases (hcp structure) usually have a cube or elliptical morphologies and serve as the nucleation sites of α phases. (3) α phases nucleate at dislocations or subgrain boundaries.[33] Dislocations can relax the lattice distortion energy and serve as a fast channel for atoms diffusion, thus, they become the preferential nucleation sites of the secondary phases. Dislocations inducing the precipitation of nano-α phases are more in line with this work by comparative analysis of the three mechanisms. Detail analysis will be shown below.

As a $\beta \rightarrow \alpha$ phase transformation, the change of crystal lattice (BCC → HCP) is closely connected with α/β stabilizers. In Figure 5(a), near the fatigue crack region, there are numerous nano-α phases precipitating

in the β phases. Figure 5(c) represents the local high magnification of the nano-α phases. The line distributions of the Ti, Al, V and O elements are shown in Figures 5(b) and (d). It can be found that the content of V element (β stabilizer) changes rapidly at the phase interface, and the V element in the (β) phase is significantly higher than primary α phase. On the contrary, the content of Al element in α phase is higher than that in β phase. However, O acts as an α stabilizer, the content in the β phase is higher than α phase. The large interspace in the β phase results in more O atoms dissolving in the voids due to the BCC structure. More importantly, as shown in Figure 5(d), there are four noticeable fluctuations in the weight fraction of V element. The positions of the fluctuations correspond to nano-α phases. The decrease of V element reduces the stability of the β phase. In addition, high temperature accelerates the diffusion of O atoms in α phase and β phases. O enhances the stability of α phase and promotes the phase transformation ($\beta \rightarrow \alpha$). Therefore, the precipitation of nano-α phases is related to the solid solution of O element and the decrease of V element.

It is equivalent to a long ageing heat treatment for holding the fatigue test sample at 723 K for 45 hours. Nevertheless, the fatigue sample experiences cyclic loading process at the same time. Previous experiments
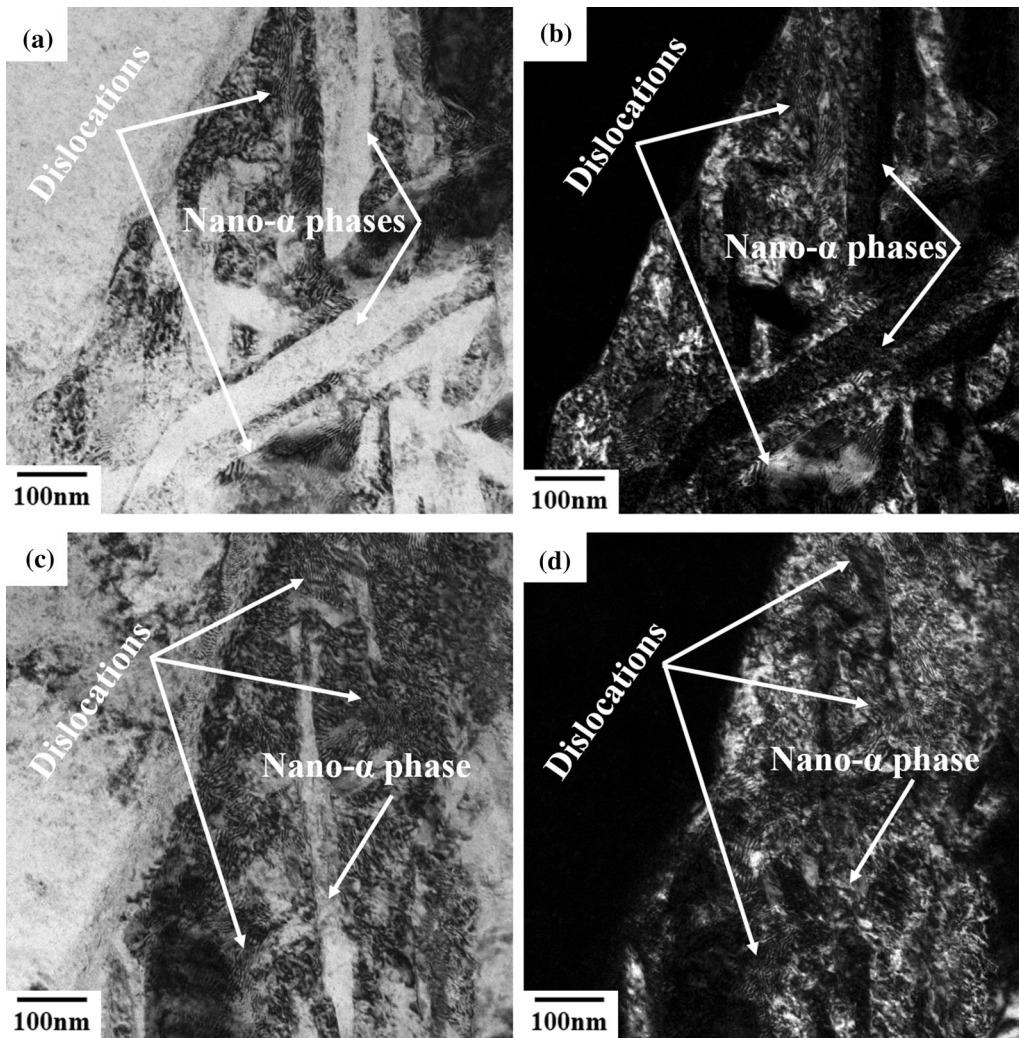
Fig. 6—Dislocations distribute in the $\beta$ phase. (a, b) The BF images of nano-$\alpha$ phase and $\beta$ phase; (c, d) The DF images of nano-$\alpha$ phase and $\beta$ phase.

have shown that **w** phases form in the $\beta$ phase if the metastable $\beta$ alloys are aged at 573 K, while **w** phases disappear with the ageing temperature increasing.[31,32] Froes *et al.*[33] have reported that **w** phase regime extends to 698K in Ti-11.5Mo-6Zr-4.5Sn alloy, and $\alpha$ phases predominate above this temperature. Moreover, the addition of Al and O would slow down the **w** formation and reduce the volume fraction of **w** phases.[34] In this work, the fatigue test is carried out at 723 K, which accelerates the diffusion of O atoms into the $\beta$-Ti. Therefore, **w** phases are difficult to form in the $\beta$ phase, moreover, **w** phases are not found through the diffraction spot analysis in the TEM images. Thus, the precipitation of nano-$\alpha$ phase is unlikely to nucleate from **w** phases.

When $\alpha$ phase nucleates at dislocation, it is coarser than that nucleates from $\beta'$ or **w** phase.[31] However, the small $\beta$ phase size and the low temperature limit the growth of $\alpha$ phase in this work. Owing to the difference in the crystal lattice structure between the HCP-$\alpha$ and BCC-$\beta$ phase, the uncoordinated strain results in numerous dislocations accumulating in the $\beta$ phases.

As shown in Figure 6, numerous dislocations distribute in the $\beta$ phase, representing that a large number of defects have been introduced into the crystal lattice, and these defects can effectively reduce the nucleation energy. In addition, the dislocation density and nano-$\alpha$ phases in Figure 6(a) (Figure 6(b)) are significantly different with those in Figure 6(c) (Figure 6(d)). Figure 6(a) presents high-content nano-$\alpha$ phases and low-density dislocations, while Figure 6(c) shows high-density dislocations and low-content nano-$\alpha$ phases. It indicates that dislocations act as the nucleation sites of nano-$\alpha$ phases, and the precipitation of nano-$\alpha$ phases effectively reduces the dislocation density in the $\beta$ phase. The V atoms diffuse faster than Al atoms in the $\beta$ phase due to the lower atomic radii (V 135 pm, Al 143 pm). The V atoms diffuse out of the crystal lattice and are gradually replaced by Al atoms and Ti atoms (Ti 147 pm). At the same time, O atoms dissolve into the crystal lattice. The large-size atoms (Al, Ti) replacing the small-size atoms (V), and the interstitial solution (O atoms) results in the crystal lattice expansion, bringing a large lattice distortion energy. However, numerous
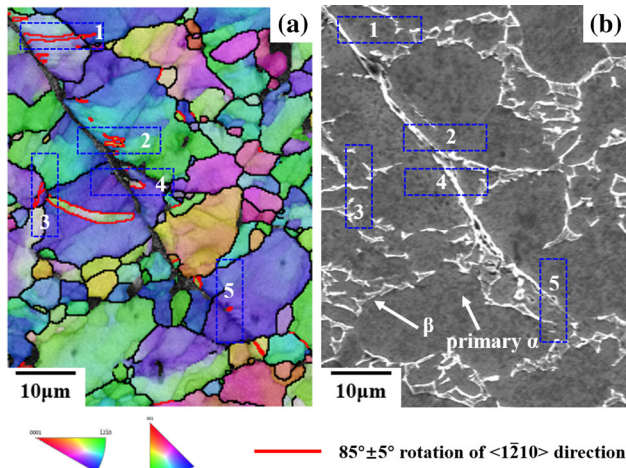
Fig. 7—EBSD map and SEM images of the fatigue crack tip. (*a*) The $\{10\bar{1}2\}$ deformation twins near the fatigue crack; (*b*) The fatigue crack propagates along the $\alpha/\beta$ interface and the primary α phase.

dislocations in the β phase can effectively balance the lattice distortion. High-density dislocation would promote the atoms diffusion, and the mutual influence of dislocation and lattice distortion accelerates the phase transformation ($\beta \rightarrow \alpha$).

It has been reported that when there are many β stabilizers, β phase can directly transform into α phase with lenticular morphology.[35] Moreover, $\beta \rightarrow \beta'$ usually takes place if the alloy compositions rich in β stabilizers and occurs at temperature above 773 K, and the addition of α stabilizers (Al, O) would reduce the stability of $\beta'$ phase and accelerate the nano-α nucleation. Therefore, considering three nucleation mechanisms, dislocations are more likely to contribute to the nano-α nucleation. The plastic deformation at the crack tip leads to numerous dislocations accumulation, and dislocations become the diffused channel (O and V atoms). The α stabilizers (O element) diffuse into the crystal lattice and β stabilizers (V element) spread out of the crystal lattice which accelerate the nano-α nucleation.

Gey *et al.*[36] have reported that $\{110\}\langle111\rangle$ and $\{112\}\langle111\rangle$ slip systems are prior to phase transformation ($\beta \rightarrow \alpha$) in hot rolled Ti-6Al-4V alloy. Qiu *et al.*[37] have investigated that dislocations have significant influences on variant selection during α precipitation in Ti-6Al-4V alloy. In their work, dislocations not only induce phase transformation, but also have a selective effect on α variants. The phase transformation strain can effectively accommodate the strain field related with dislocations.[38] As well known, the energy during the phase transformation process includes chemical free energy, elastic strain energy and applied force field. When there is a negative interaction between these energies, it would effectively weaken the stress field related with dislocations, thereby promoting the nano-α nucleation. In addition, the system can reach a stable equilibrium state when the sum of the surface energy and strain energy is minimum. To make the strain energy minimum, the secondary phases tend to form plates or flakes. While to make the surface energy minimum, the secondary phases show equiaxed morphology. Therefore, nano-α phases precipitate with lenticular morphology in the competition of surface energy and strain energy.

### C. *The Nucleation and Propagation of $\{10\bar{1}2\}$ Deformation Twins*

Figure 7 shows the $\{10\bar{1}2\}$ deformation twins at the crack tip region. It can be found that there are four cases of the nucleation and propagation of deformation twins. (1) The paired twins ($T + T$) grow across the primary α/β interface (area 1). The twin boundaries (TBs) are discontinuous at the interface. (2) Adjacent twins nucleate at the LAGBs (area 2) and grow across the LAGBs. (3) The twins nucleate at the primary α/β interface (area 3) and grow into the primary α grains. (4) The twins nucleate in the primary grains and fatigue crack propagates through the deformation twins (area 4, 5).

The twin nucleation divides into homogeneous and heterogeneous mechanisms.[39] Homogeneous nucleation takes place in the parent grains with hard orientation of slip system. Crystal slip is not enough to accommodate plastic deformation leading to the local stress concentration in hard grains and twin nucleation.[40,41] It is necessary to reach the CRSS for twin nucleation, thus, twins nucleate preferentially in the grains with low SF of slip system ($SF_{slip}$) but high SF of twin system ($SF_{twin}$). Heterogeneous nucleation is attributed to the result of dislocation reactions.[42] The decomposition of a pre-existing dislocation into twinning dislocations thereby promoting the nucleation of deformation twins. From Figure 8, it can be found that the parent grains do not conform to the characteristics of low $SF_{slip}$ and high $SF_{twin}$, on the contrary, the parent grains have similar SF values (0.2 to 0.4) of different slip systems and $\{10\bar{1}2\}$ twin system. In the local misorientation (LocMis) map (Figure 8(a)), the LocMis value represents the nonuniform strain, which can be regarded as a measurement of geometrically necessary dislocations (GNDs). High strain gradients indicate a dense dislocation accumutation, causing the increase of the flow stress according to the Taylor's theory.

The dislocations dissociate into twinning dislocations, and the slide of twinning dislocations results in the nucleation and propagation of deformation twins. Two beams diffraction TEM technique is carried out to identify the dislocation types in the grains and α/β interface (Figure 9). The dense dislocations are out of contrast under the 0001 g-vector (Figure 9(b)) but are visible with the $1\bar{1}01$ g-vector (Figure 9(c)) and $1\bar{1}00$ g-vector (Figure 9(d)), which indicate that the dense dislocations consist of <*a*> dislocations. <*a*> dislocations are invisible while <*c* + *a*> dislocations are visible under the 0001 g-vector. Thus, the visible dislocations in Figure 9(b) presumably consist of <*c* + *a*> dislocations. It can be found that <*a*> dislocations and <*c* + *a*> dislocations pile up at the primary α/β interface. Stress
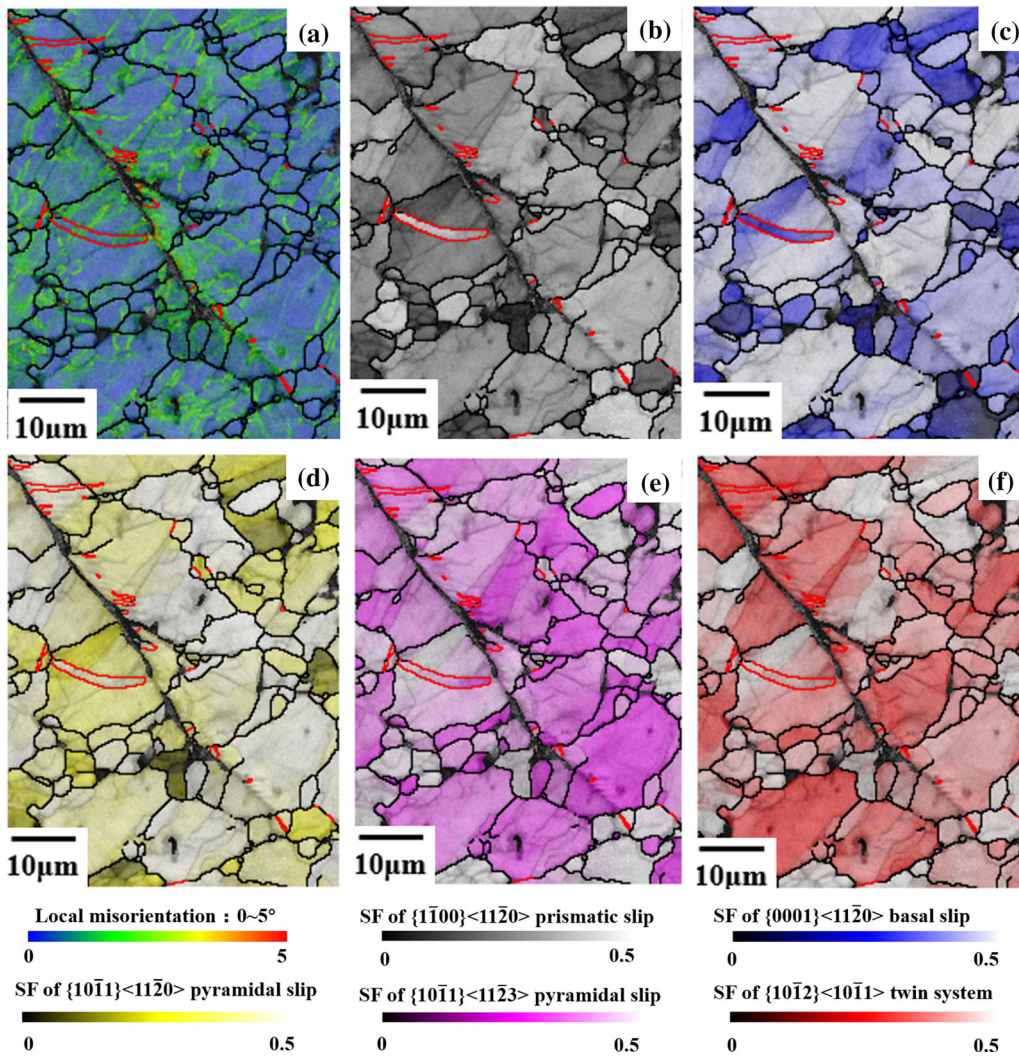
Fig. 8—EBSD maps of $\{10\bar{1}2\}$ deformation twins. (a) local misorientation map; (b) SF map of prismatic slip; (c) SF map of basal slip; (d) SF map of pyramidal $<a>$ slip; (e) SF map of pyramidal $<c + a>$ slip; (f) SF map of $\{10\bar{1}2\}$ twin system.

concentration at the interface would result in the dissociating of dislocations.

Several factors would lead to stress concentration: (1) Dislocations in the primary α grains accumulating at the interface; (2) Dislocations in the β phase piling up at the interface; (3) Dislocations at the tip of lenticular nano-α phases blocking at the interface (Figure 10); (4) The stress field at the tip of fatigue crack caused by the applied force. The $<a>$ ($1/3[\bar{1}\bar{1}20]$ or $1/3[1\bar{2}10]$) dislocations in the primary α grains accumulating at the interface, which work as the twinning dislocation source by dissociating into a residual dislocation $b_r$ and twinning dislocations $b_t$ ($\frac{3-\gamma^2}{3+\gamma^2}<\bar{1}011>$) [24]:

$$a_2 \ or \ a_3 \rightarrow b_r + 3b_t \quad [1]$$

$$a_2 \rightarrow b_r + b_t \quad [2]$$

For α-Ti, $a = 0.295$ nm, $c = 0.468$ nm, $\gamma = c/a$. The above dislocation transmutations are energetically favorable due to $|a|^2 > |b_r|^2 + |3b_t|^2$ and $|a_2|^2 > |b_r|^2 + |b_t|^2$

The $<c + a>$ ($1/3[\bar{1}2\bar{1}3]$) dislocations can dissociate into $<c>$ ($[0001]$) dislocations and $<a>$ ($1/3[\bar{1}2\bar{1}0]$) dislocations[43,44]:

$$<c + a> \ \rightarrow \ <c> \ + \ <a> \quad [3]$$

This dislocation transmutation seems that no reduction occurs in the elastic strain energy because of $|c + a|^2 = |c|^2 + |a|^2$ which is non-conformance with Frank's law. However, it has been confirmed that there is a smaller reduction in the total dislocations energy.[44] In addition, the dissociation $<c + a> \rightarrow <c> + <a>$ is the dominant decomposition at high loading. Therefore, the strong stress field at the crack tip is likely to result in the dislocation reaction. The dissociated $<a>$ from the $<c + a>$ dislocations would become a source of twinning dislocations again. Figure 11 shows the diagram of $<a>$ and $<c + a>$ dislocations dissociate into twinning dislocations. The dislocation transmutations result in
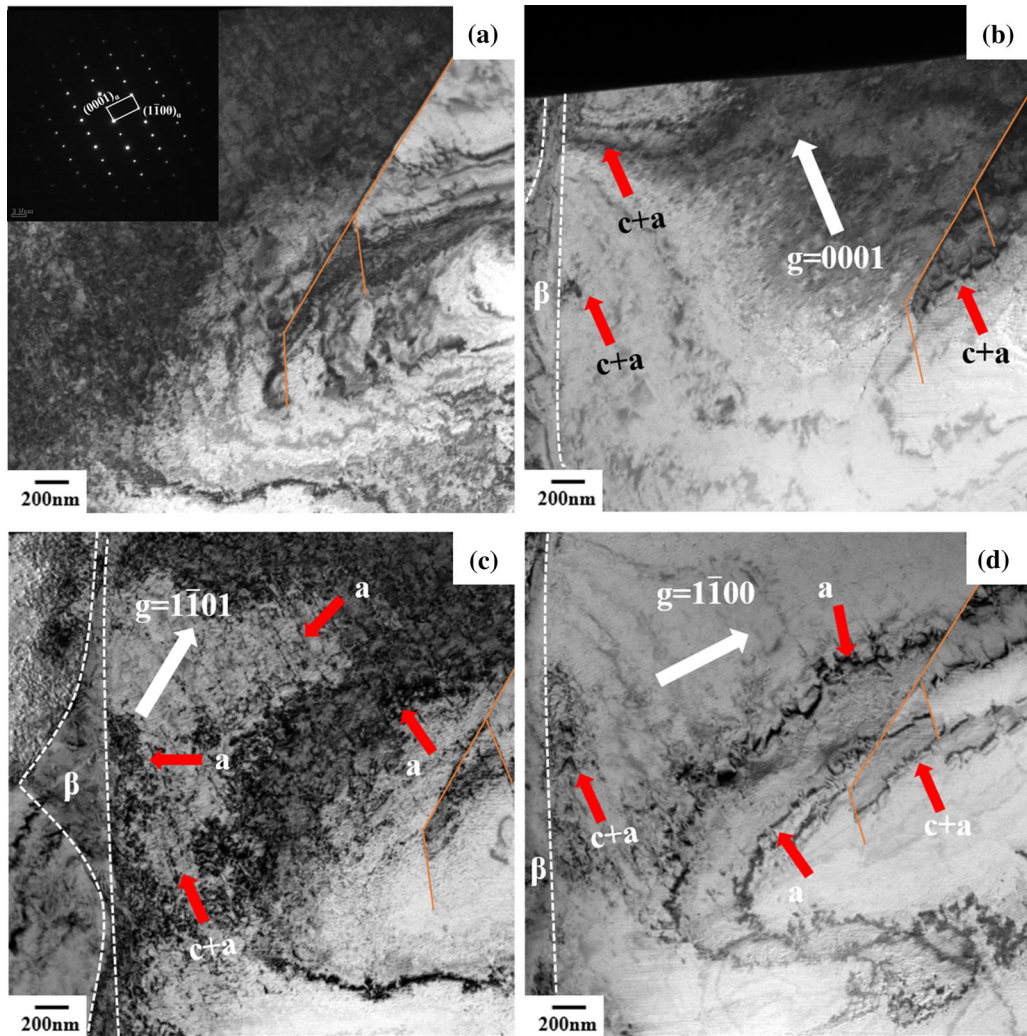
Fig. 9—BF TEM images under two-beam condition. (*a*) The region of operating area; (*b*) $g = 0001$; (*c*) $g = 1\bar{1}01$; (*d*) $g = 1\bar{1}00$.
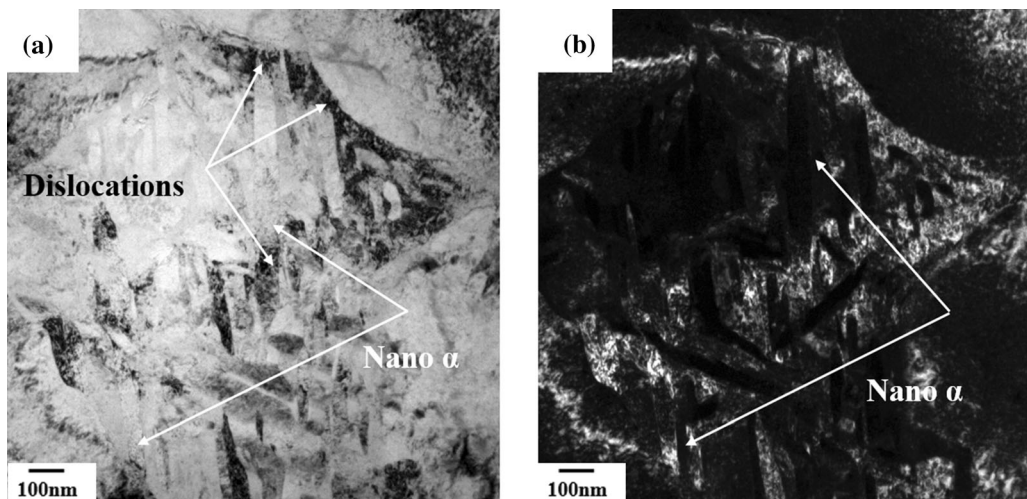


Fig. 10—Dislocations pile up at the tip of nano-α phases. (*a*) The BF image; (*b*) The DF image.

the formation of twinning dislocations and the plastic deformation at the crack tip leads to the twinning dislocation slip, which lead to the nucleation and propagation of deformation twins.

As discussed above, numerous nano-$\alpha$ phases precipitate in the $\beta$ phases. Several literatures have been reported that the $\alpha$ phases are $\{10\bar{1}2\}\langle10\bar{1}1\rangle$ twins, which precipitated in the $\beta$ titanium alloy during the ageing process.[35] Part of twins have OR $(0002)_\alpha$ $//\{101\}_\beta$ and $\langle2\bar{1}\bar{1}0\rangle_\alpha//$ $\langle111\rangle_\beta$ with $\beta$ phase, and some twins do not have this same OR. The results of this work (Section III–A) are consistent with the work in the literature.[35] Thus, it can be inferred that nano-$\alpha$ phases are $\{10\bar{1}2\}\langle10\bar{1}1\rangle$ twins in this work. The nano-$\alpha/\beta$ interface shows terraced structure (Figure 3(d)) which consists of terrace planes and ledge planes. According to the theory of diffusion phase transformation, the length of nano-$\alpha$ phase is controlled by the interfacial concentration, and the increased thickness of nano-$\alpha$ phase is attributed to



Fig. 11—The diagram of <a> dislocations and <c + a> dislocations dissociate into twinning dislocations. (a) The transmutation of <a> dislocations; (b) The transmutation of <c + a> dislocations.

ledge growing. As shown in Figure 12, nano-$\alpha$ phase precipitates in the $\beta$ phase and the orientation of $\beta$ phase on both sides of $\alpha$ phase changes slightly due to the growth of nano-$\alpha$ phase. Moreover, nano-$\alpha$ phases extend to the primary $\alpha/\beta$ interface, and the dislocations pile up at the interface. Owing to the stress field at the crack tip and the interaction between nano-$\alpha$ phases and primary $\alpha/\beta$ interface, numerous dislocations accumulate at the interface during the cycle loading process. When the twinning dislocations at the tip of nano-$\alpha$ phases transmute into dislocations in the $\beta$ phase and then convert to twinning dislocations in primary $\alpha$ phases, the nano-twins would cross the primary $\alpha/\beta$ interface and propagate in the primary $\alpha$ phase. The ability of dislocations transformation can be calculated by the equation $m = \cos(90\times\theta_i/\theta_c)\times\cos(90\times\psi_i/\psi_c)$, where $\theta_i$ is the angle of intersection lines between the nano-twin and $\beta$ phase with interface, and $\psi_i$ is the angle of slip directions. Moreover, $\theta_c$ and $\psi_c$ are the critical values which are 15 deg and 45 deg, $\theta_i$ and $\psi_i$ are required to be not higher than these critical values.[24,45,46] The twinning dislocation transformation is much easier when the $m$ is higher. There are six variants of $\{10\bar{1}2\}$ twins, and there is no specific OR between primary $\alpha$ phase and $\beta$ phase, once their orientation ($m \geq 0.25$)[44] facilitates the dislocations transform process, the nano-twins would pass through the primary $\alpha/\beta$ interface and grow in the primary $\alpha$ phases.

However, achieving twinning dislocation conversion is relatively difficult due to the limitation of orientation. It's less probable to propagate into the primary $\alpha$ phase for lots of nano-twins. Strain transferring may cause the twin nucleation in the primary $\alpha$ phase when dislocations cannot slide through the interface. Wang et al.[16] have reported paired twins nucleate at GBs in titanium. They concluded that the $T + T$ is a process of strain transfer across GBs. The strain compatibility factor $\lambda = \cos\Phi \times \cos\kappa$ can be used to represent the ability of strain transferring between two adjacent twins, where $\Phi$ is the
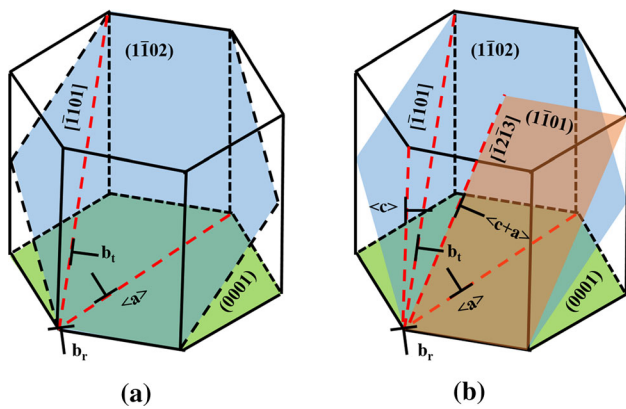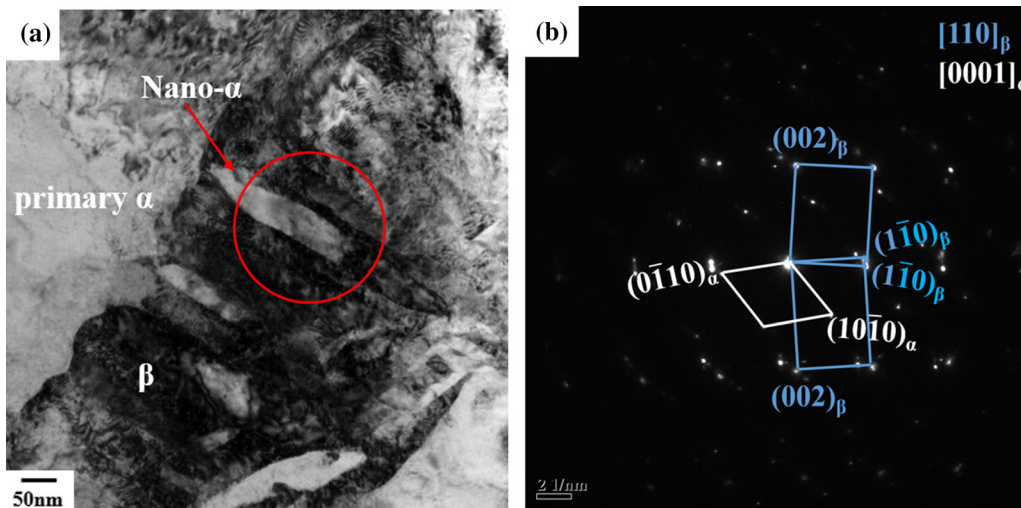


Fig. 12—Orientation difference in $\beta$ phase on both sides of nano-$\alpha$ phase caused by the growth of nano-$\alpha$. (a) BF TEM micrograph; (b) The SAED pattern taken along $[0001]_\alpha//[110]_\beta$ from the red circle.
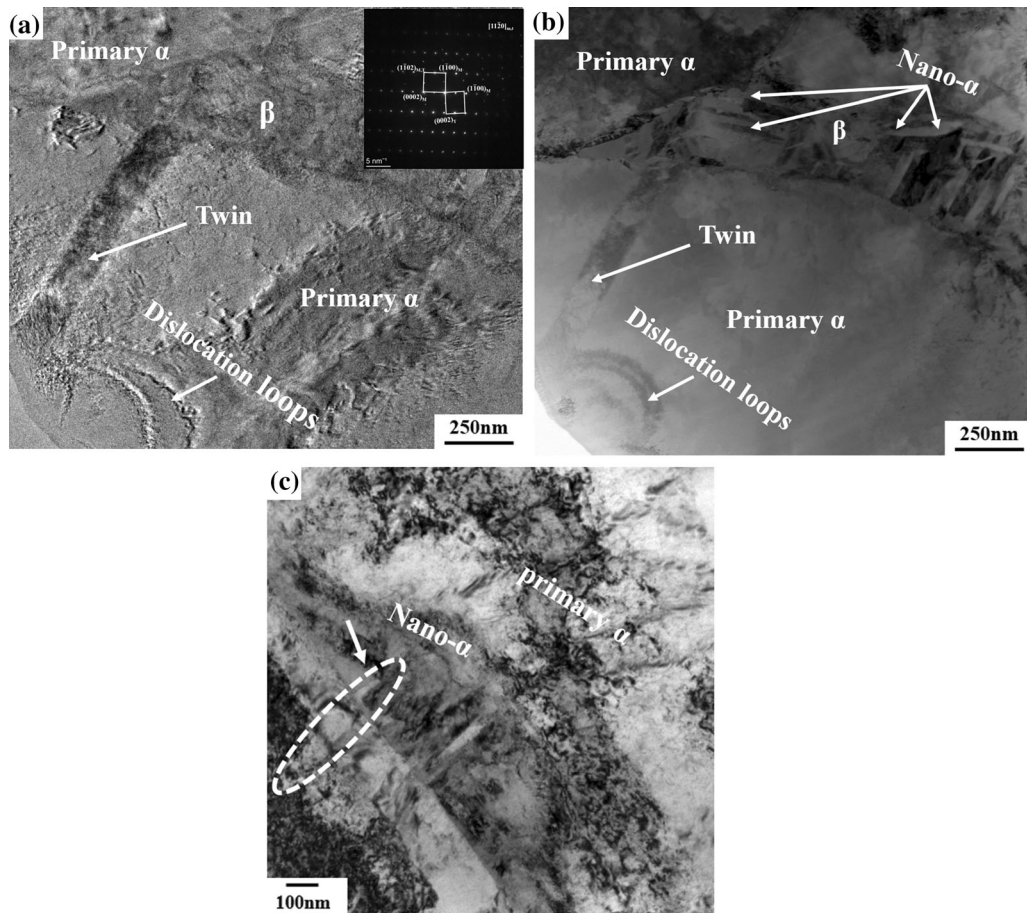
Fig. 13—Examples of twin and nano-α propagate into primary α phase. (a, b) $(1\bar{1}02)$ deformation twin propagates from β phase into primary α phase; (c) Nano-α phase propagates from β phase into primary α phase.

angle between twin plane normal and $\kappa$ is the angle between twin shear directions.[16,47] The twin nucleation occurs in the neighboring grains to relax the stress at the twin tip when the primary twin halt at GBs.[47] Similarly, the strain may transfer into the primary α phase when numerous dislocations pile up at the interface. The nano-α twins spread over the interface by autocatalytic-type reaction, and result in new twins nucleating at the adjacent primary α GBs and achieving the stress-relaxation at the interface. To achieve effective strain transfer, the new twins should have a good strain transfer ability, therefore, it is possible to activate the same twin variants $(\Phi = 0, \kappa = 0, \lambda = 1)$.

It can be found that $(1\bar{1}02)$ deformation twin seems to nucleate in the β phase, crossing the primary α/β interface, and growing into the primary α phase (Figure 13(a)). As shown in Figure 13(b), numerous nano-α phases distribute around the deformation twin. The twinning dislocations transformation may result in the propagation of $(1\bar{1}02)$ twin in the primary α phase. Moreover, the lenticular nano-α phase with continuous boundary (Figure 13(c)) propagates into the primary α phase on both sides of the β phase, which illustrates the possibility of the conversion of twinning dislocation. In addition, paired $\{10\bar{1}2\}$ deformation twins with discontinuous boundaries nucleate at the phase boundaries

(the area 1 in Figure 7(a)) which proves the possibility of new twin nucleation by strain transfer. These results can strongly prove that twinning dislocations transformation and strain transferring promote the nucleation and propagation of $\{10\bar{1}2\}$ deformation twins in the primary α phases.

In summary, there are two mechanisms for the twin nucleation: (1) As shown in Figures 14(a) and (b), dislocations dissociate into twinning dislocations and deformation twins nucleate at GBs and LAGBs; (2) As shown in Figure 14(c), nano-α twins result in strain transferring at the interface and promote the new twin nucleation in the primary α phase. In addition, the twinning dislocations transformation would lead to the nano-α twins break through the α/β interface and propagate in the primary α phases (Figure 14(d)).

D. *Effects of Microstructural Evolution on the Fatigue Crack Propagation*

Figure 15 shows the crack propagation path and fatigue fracture morphology of Ti-6Al-4V alloy after high-temperature fatigue test. Notably, the crack propagation direction is almost perpendicular to the loading direction. Crack propagates along the α/β interfaces or across the primary α phases. The early fatigue crack
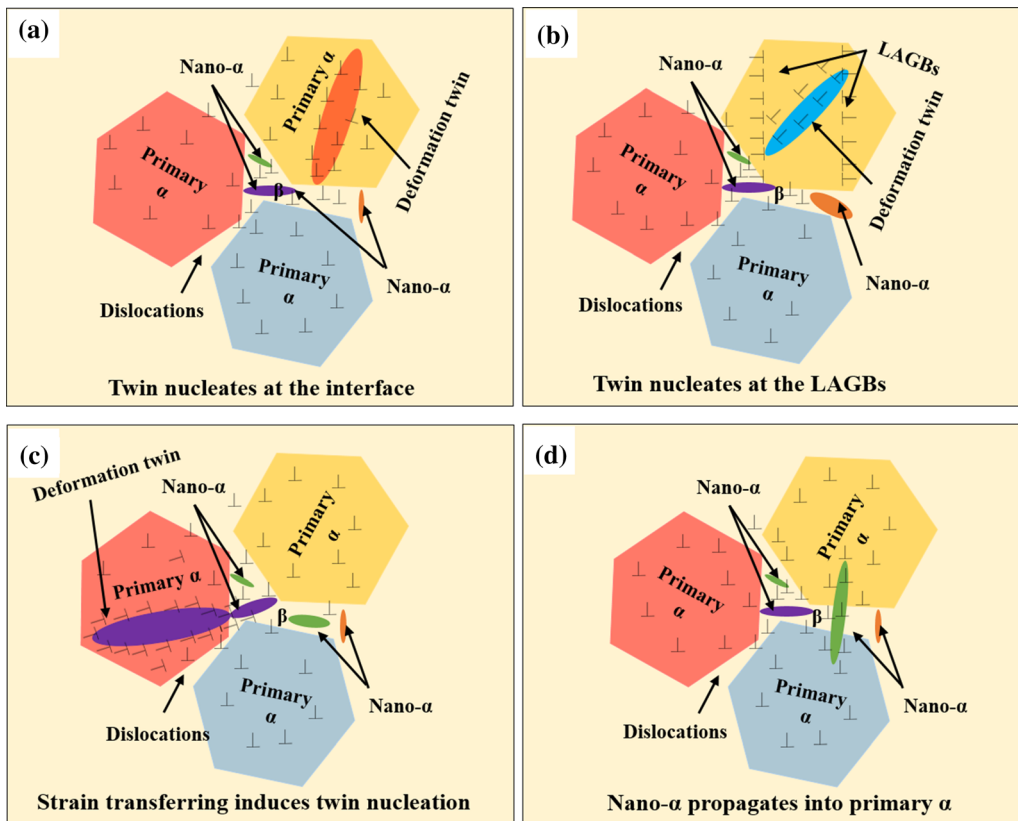
Fig. 14—The schematic diagram of twin nucleation and propagating through the interface. (*a*) Twin nucleates at the interface by dislocations dissociating into twinning dislocations; (*b*) Twin nucleates at the LAGBs by dislocations dissociating into twinning dislocations; (*c*) Nano-α blocks at the interface and strain transferring induces twin nucleation at the adjacent primary α; (*d*) Nano-α propagates into the primary by twinning dislocation transformation.

(Figure 15(a)) experiences severe plastic deformation due to long-term loading, and mainly spread through the primary α phases, and the undulating crack surface indicates the existence of roughness-induced crack closure mechanism. New crack nearby the crack tip (Figure 15(c)) mostly propagates along the α/β interfaces or along the path with a relatively large number of β phases after holding at 723 K for 45 h, and secondary cracks occur along the main crack. This may be related to nano-α phases increasing the heterogeneity, and twins has an effect on the crack propagation. The fatigue striations (Figure 15(b)) indicate that amplitude of stress intensity factor ($\Delta K$ = 10 MP m$^{1/2}$) corresponds to the second stage of fatigue crack growth. While the appearance of transgranular cracks and intergranular cracks proves that $\Delta K$ is close to the threshold of amplitude of stress intensity factor ($\Delta K_{th}$), thus, adjacent striations are relatively small (approximately 0.25 $\mu$m) (Figure 15(d)).

Figure 16 shows the EBSD maps of fatigue test Ti-6Al-4V specimen. The fatigue crack mainly propagates through the grains, and there are numerous LAGBs (2 deg to 10 deg) (red GBs) distributing in the specimen. The fraction of LAGBs increases by 20 pct after fatigue test. Moreover, {10$\bar{1}$2} deformation twins (white TBs) form in the fatigue test sample. As mentioned in the introduction, the CTPZ size is about 50

$\mu$m, thus, the plastic deformation occurs in the grains at the fatigue crack tip, and cyclic deformation causes numerous dislocations to form LAGBs.

Figure 17 shows the fatigue crack growth rate (FCGR) of Ti-6Al4V alloy compared with literatures,[10,12,48,49] and the FCGRs are corresponding to $\Delta K$ = 10 MP m$^{1/2}$ with different stress ratios or the same rate under different fatigue conditions. In Figure 17(a), by fitting the crack length-time curve, the $R$-square is close to 1, indicating that the crack length increases linearly with time during the fatigue test, and it also proves that the accuracy of DCPD method to measure the FCGR of titanium alloy under constant $\Delta K$. It is difficult to quantitative compare the FCGRs of Ti-6Al-4V due to the diversity of fatigue test conditions. However, Sanders et al.[50] have reported that the FCGR is almost independent of the loading frequency when the temperature is below 673 K, but the FCGR decreases as the loading frequency increases when the temperature is above 673 Noroozi et al.[51] have found that the FCGR of Ti-6Al-4V alloy increases with the stress ratio decreasing, and with the test temperature increasing, the decrease in elastic modulus and yield strength would result in an increase in the plastic zone of the crack tip and accelerate fatigue crack propagation.[52] The enhanced oxidation leads to the increase of crack closure effect, and the actual stress intensity factor
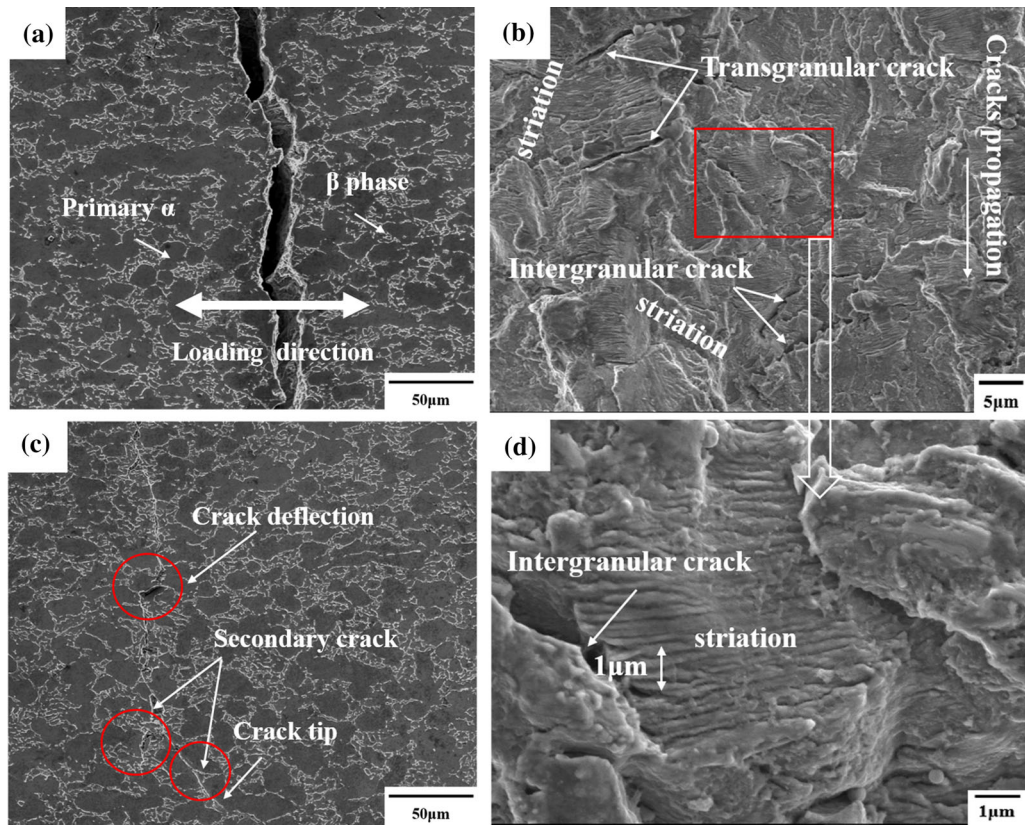
Fig. 15—SEM images of the fatigue crack paths and fracture morphology after high temperature fatigue. (*a*) early fatigue crack path; (*b*) fatigue morphology (low magnification); (*c*) fatigue crack path nearby crack tip; (*d*) fatigue morphology (high magnification of (b)).

decreases at the crack tip, which results in the reduction of FCGR.[53] Therefore, as shown in Figure 17(b), compared with other work, the FCGR in this work is relatively lower.

From Figure 15, there is less oxide on the fatigue fracture surface, thus, the effect of oxide-induced crack closure on the FCGR is lower. As discussed above, nano-α phases and deformation twins are newly found in Ti-6Al-4V alloy during high-temperature fatigue test. Singh *et al.*[11] have reported that low cycle fatigue would result in the growth of the pre-existing $Ti_3Al$ at 873 K, and lead to the precipitation of fresh $Ti_3Al$ phase, and cause the strengthening effect on Timetal 834 alloy. In this work, the precipitation of nano-α phases, the formation of $\{10\bar{1}2\}$ deformation twins and the occurrence of numerous LAGBs have important effects on the propagation of fatigue cracks. For nano-α phase: (1) since interfaces are the preferred sites for crack nucleation, more nano-α/β interfaces form in the β phase, more crack sources are introduced to accelerate the FCG. (2) The precipitation of nano-α phases increases the heterogeneity of microstructures, stress concentration is more likely to occur at the primary α/β interface, and result in the interfacial crack. Secondary crack may nucleate near the nano-α phase and primary α/β interface (Figure 18(a)). (3) The β grain size is refined due to the formation of nano-α phases. Precipitation strengthening and grain refinement would bring about an increase in

tensile strength,[30] which leads to the reduction of plastic zone at the crack tip, thus, it's conducive to ease the fatigue crack propagation. For LAGBs: (1) It has been reported that LAGBs are the strongest in resisting fatigue cracking, high angle grain boundaries (HAGBs) are the weakest, the ability of TBs to hinder crack propagation is in between.[54] A large number of LAGBs become the important resistance to the crack propagation, thereby LAGBs effectively weaken the FCG (Figure 18(b)). (2) The fatigue crack grows by the emission of dislocations in the front of crack tip.[55] Part of the dislocations can be absorbed by the LAGBs, thus, crack growth is inhibited by the LAGBs. In addition, as shown in Figure 16(b), the secondary crack gradually becomes the main crack, and the crack propagates along a route where numerous twins are distributed. Therefore, deformation twins play key roles on crack propagation: (1) Twins work as a barrier to dislocation movement, which would effectively prevent dislocation slip and slow down FCGR. (2) Twins change the local orientation of the parent grain, which can deflect the crack propagation direction, thereby consuming more energy and reducing the driving force of the crack growth.[53] (3) The formation of $\{10\bar{1}2\}$ twin would affect the cohesive properties of GBs and result in its fatigue cracking.[21] Above all, the integrative effects of nano-α phase, LAGBs and deformation twins result in the decrease of the FCGR of Ti-6Al-4V alloy.
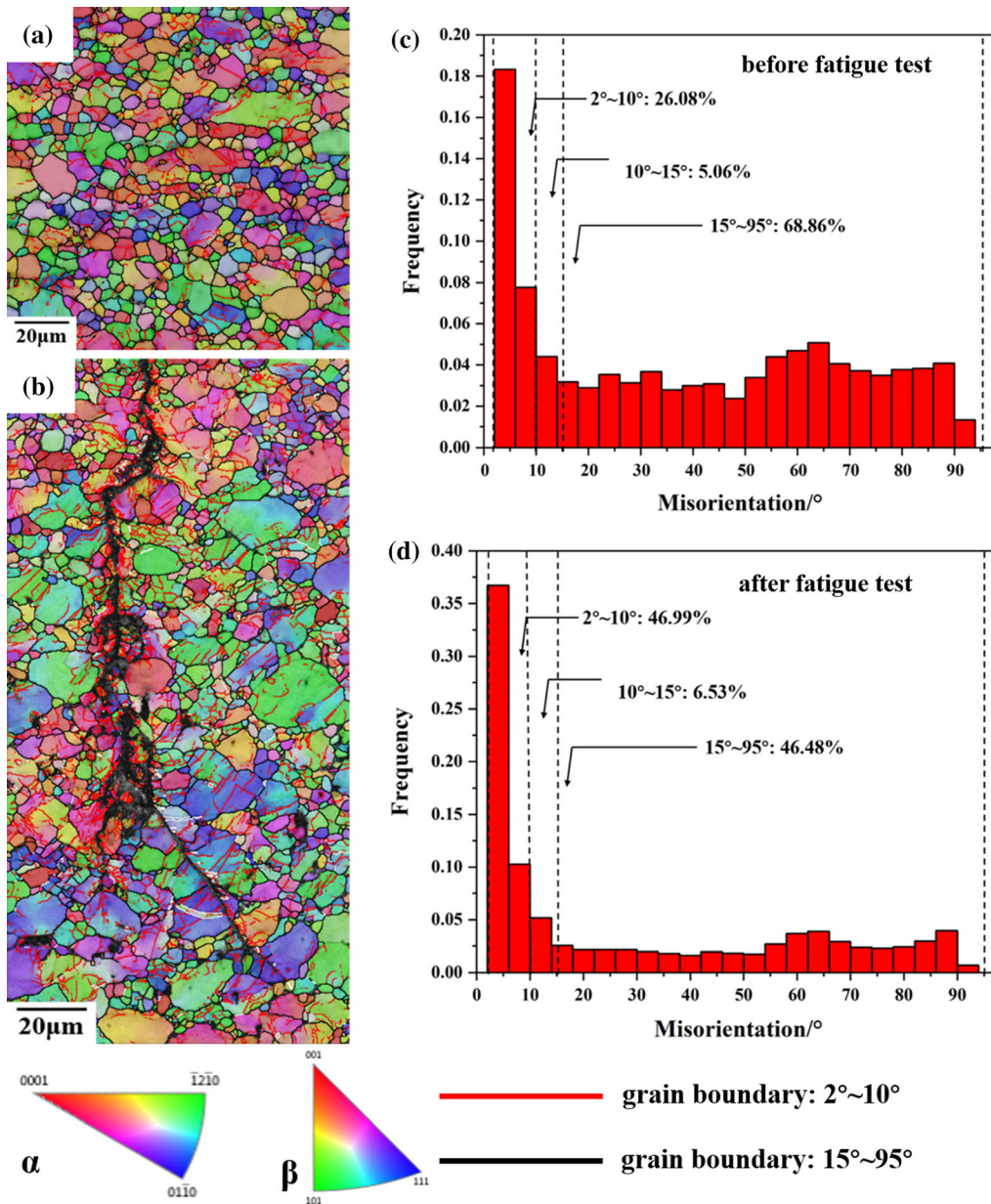
Fig. 16—EBSD maps of fatigue test Ti-6Al-4V specimen. (*a*) IPF map and grain boundary distribution map before fatigue test; (*b*) IPF map and grain boundary distribution map after fatigue test; (*c*) The histogram of grain boundary misorientation before fatigue test; (*d*) The histogram of grain boundary misorientation after fatigue test.

## IV. CONCLUSIONS

In this work, we discussed exceptional nano-α phases and $\{10\bar{1}2\}$ deformation twins in Ti-6Al-4V alloy with equiaxed microstructure during high-temperature fatigue test. The ORs between nano-α and β phase, precipitation mechanism of nano-α phases, the twin nucleation and propagation mechanism are systematic discussed. The main conclusions are as follows:

(1) Exceptional nano-α phases precipitate in the β phase and have $(0001)_\alpha//(110)_\beta$, $[11\bar{2}0]_\alpha//[111]_\beta$ Burgers orientation relationship (OR) with β phase, the nano-α/β interface with terraced

structure consists of $(0\bar{1}10)_\alpha//(1\bar{1}2)_\beta$ and $(10\bar{1}0)_\alpha//(1\bar{1}0)_\beta$.

(2) Numerous dislocations accumulate in the β phase. Dislocations become the diffused channel of O, Al and V atoms. The α stabilizers (O element) diffuse into the crystal lattice and β stabilizers (V element) spread out of the crystal lattice which accelerate the nucleation of nano-α phases.

(3) The nucleation of $\{10\bar{1}2\}$ deformation twins is attributed to heterogeneous mechanisms. <*a*> and <*c* + *a*> dislocations pile up at the primary α grain, interface and LAGBs, dissociate into twinning dislocations and promote the twin nucleation.
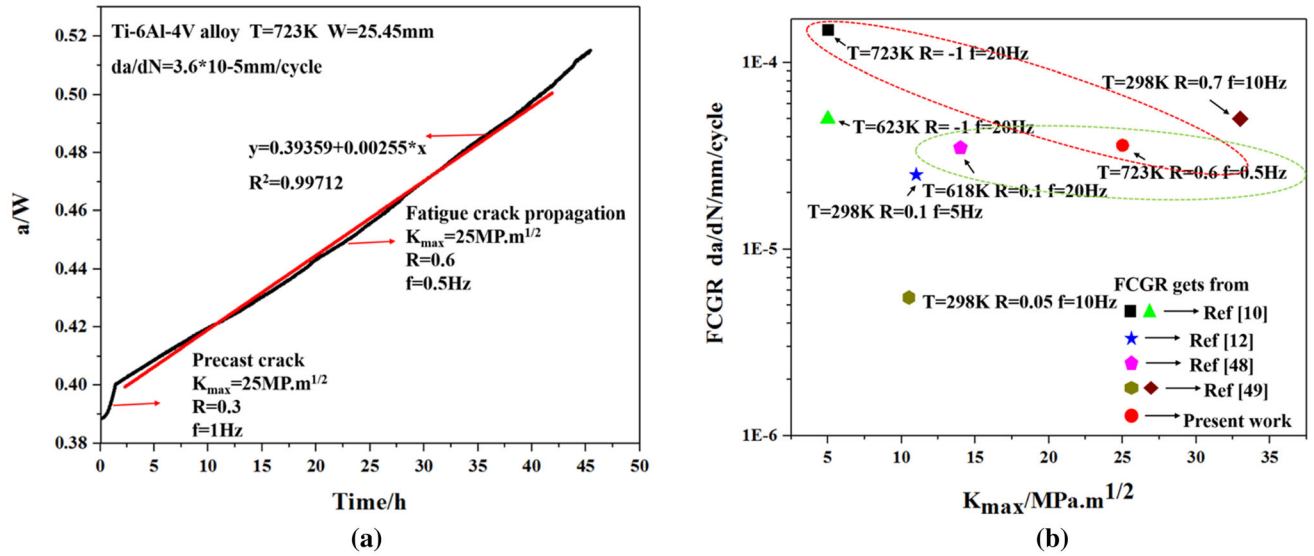
Fig. 17—The FCGRs of Ti-6Al-4V alloy. (*a*) The curve of Time-Crack length; (*b*) Comparison of FCGRs with literatures.
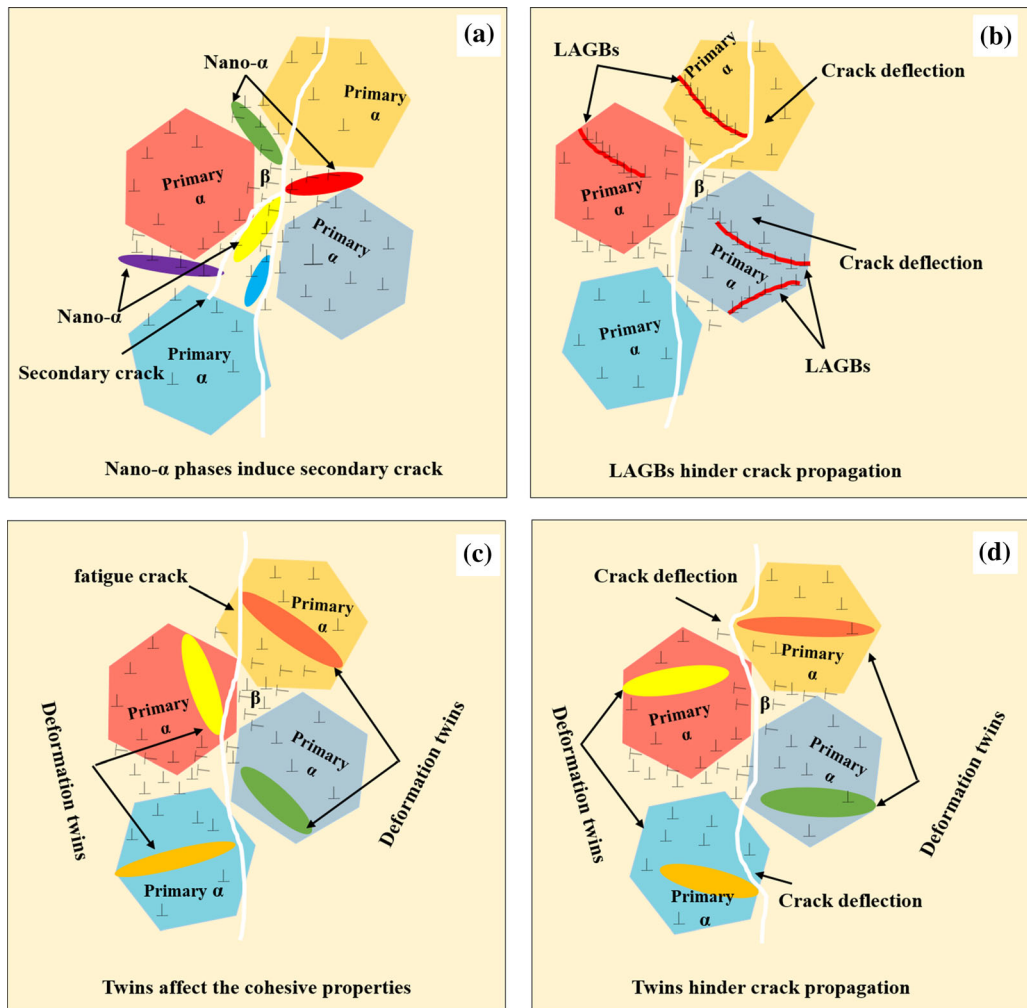


Fig. 18—The schematic diagram of the effects of microstructure evolution on crack propagation. (*a*) Nano-α phases increase the microstructure inhomogeneity and induce secondary cracks; (*b*) LAGBs hinder the crack propagation and result in crack deflection; (*c*) Twins affect the cohesive properties of twin/matrix interface and lead to crack propagating along the twins; (*d*) The direction of crack propagation is perpendicular to the twin axis, twins hinder the crack propagation and deflect the crack propagation.

(4) The twinning dislocations transformation would help the nano-α twins cross the α/β interface and propagate in the primary α phase. Moreover, nano-α twins would result in strain transfer at the interface and promote the new twin nucleation in the adjacent primary α grain.

(5) The nano-α phases, deformation twins and low angle grain boundaries play key roles in fatigue crack propagation. With the effects of nano-α phases, LAGBs and twins, the resistance of crack propagation increased and the driving force decreased, and result in the low fatigue crack growth rate.

## REFERENCES

1. R. Banerjee and J.C. Williams: *Acta Mater.*, 2013, vol. 61, pp. 844–79.
2. J.C. Williams and E.A. Starke: *Acta Mater.*, 2003, vol. 51, pp. 5775–99.
3. Y.M. Ren, X. Lin, X. Fu, H. Tan, J. Chen, and W.D. Huang: *Acta Mater.*, 2017, vol. 132, pp. 82–95.
4. F. Briffod, A. Bleuset, T. Shiraiwa, and M. Enoki: *Acta Mater.*, 2019, vol. 177, pp. 56–67.
5. Y. Mine, S. Katashima, R. Ding, P. Bowen, and K. Takashima: *Scr. Mater.*, 2019, vol. 165, pp. 107–11.
6. C. Lavogiez, S. Hémery, and P. Villechaise: *Scr. Mater.*, 2020, vol. 183, pp. 117–21.
7. J.H. Zuo, Z.G. Wang, and E.H. Han: *Mater. Sci. Eng. A*, 2008, vol. 473, pp. 147–52.
8. J.S. Jha, S. Dhala, S.P. Toppo, R.S. Singh, and A. Tewari: *Mater. Charact.*, 2019, vol. 155, p. 109829.
9. X.L. Liu, C. Sun, and Y. Hong: *Mater. Sci. Eng. A*, 2015, vol. 622, pp. 228–35.
10. K. Tokaji: *Scr. Mater.*, 2006, vol. 54, pp. 2143–48.
11. N.S. Gouthama and V. Singh: *Int. J. Fatigue*, 2007, vol. 29, pp. 843–51.
12. N.K. Arakere, T. Goswami, J. Krohn, and N. Ramachandran: *High Temp. Mater. Processes*, 2002, vol. 21, pp. 229–36.
13. M.P. Echlin, J. CharlesStinville, V.M. Miller, W.C. Lenthe, and T.M. Pollock: *Acta Mater.*, 2016, vol. 52, pp. 164–75.
14. P.D. Littlewood and A.J. Wilkinson: *Acta Mater.*, 2012, vol. 60, pp. 5516–25.
15. S. Xu, M. Gong, Y. Jiang, C. Schuman, J. Lecomte, and J. Wang: *Acta Mater.*, 2018, vol. 152, pp. 58–76.
16. L. Wang, P. Eisenlohr, Y. Yang, T.R. Bieler, and M.A. Crimp: *Scr. Mater.*, 2010, vol. 63, pp. 827–30.
17. H. Qin, J.J. Jonas, H.B. Yu, N. Brodusch, R. Gauvin, and X.Y. Zhang: *Acta Mater.*, 2014, vol. 71, pp. 293–305.
18. N.P. Gurao, R. Kapoor, and S. Suwas: *Acta Mater.*, 2011, vol. 59, pp. 3431–46.
19. S. Xu, P. Zhou, G. Liu, D. Xiao, M. Gong, and J. Wang: *Acta Mater.*, 2019, vol. 165, pp. 547–60.
20. A. Ishii, J. Li, and S. Ogata: *Int. J. Plast.*, 2016, vol. 82, pp. 32–43.
21. N. Bosh, C. Müller, and H. Mozaffari-Jovein: *Mater. Charact.*, 2019, vol. 155, p. 109810.
22. A. Fitzner, D.G. Leo Prakash, J.Q. da Fonseca, M. Thomas, S. Zhang, J. Kelleher, P. Manuel, and M. Preuss: *Acta Mater.*, 2016, vol. 103, pp. 341–51.
23. E. Wielewski, C.R. Siviour, and N. Petrinic: *Scr. Mater.*, 2012, vol. 67, pp. 229–32.
24. X.D. Zheng, S.J. Zheng, J. Wang, Y.J. Ma, H. Wang, Y.T. Zhou, X.H. Shao, B. Zhang, J.F. Lei, R. Yang, and X.L. Ma: *Acta Mater.*, 2019, vol. 181, pp. 479–90.
25. A. Chapuis and J.H. Driver: *Acta Mater.*, 2011, vol. 59, pp. 1986–94.
26. G.G. Yapici, I. Karaman, and Z.P. Luo: *Acta Mater.*, 2006, vol. 54, pp. 3755–71.
27. R.W. Hertzberg, R.P. Vinci, and J.L. Hertzberg: *Deformation and Fracture Mechanics of Engineering Materials*, 5th ed., Wiley, Hoboken, 2012.
28. D. Bhattacharyya, G.B. Viswanathan, R. Denkenberger, D. Furrer, and H.L. Fraser: *Acta Mater.*, 2003, vol. 51, pp. 4679–91.
29. T. Sakamoto, Y. Higaki, S. Kobayashi, and K. Nakai: *Mater. Sci. Forum*, 2010, vols. 638–642, pp. 461–64.
30. T. Sakamoto, K. Takiue, Y. Higaki, S. Kobayashi, and K. Nakai: *Mater. Trans.*, 2017, vol. 58, pp. 986–92.
31. F. Prima, P. Vermaut, G. Texier, D. Ansel, and T. Gloriant: *Scr. Mater.*, 2006, vol. 54, pp. 645–48.
32. J. Debuigne and F. Prima: *Mater. Trans.*, 2005, vol. 46, pp. 1433–35.
33. F.H. Froes, C.F. Yolton, J.M. Capenos, M.G.H. Wells, and J.C. Williams: *Mater. Trans.*, 1980, vol. 11, pp. 21–31.
34. K. Yamada, A. Ogawa, C. Ouchi, and E. Daniel: *Mater. Trans.*, 2007, vol. 37, pp. 855–59.
35. C.G. Rhodes and J.C. Williams: *Mater. Trans.*, 1975, vol. 6, pp. 2103–14.
36. N. Gey, M. Humbert, M. Philippe, and Y. Combres: *Mater. Sci. Eng. A*, 1997, vol. 230, pp. 68–74.
37. D. Qiu, R. Shi, D. Zhang, W. Lu, and Y. Wang: *Acta Mater.*, 2015, vol. 88, pp. 218–31.
38. Z. Feng, Y. Yang, B. Huang, X. Luo, M. Li, M. Han, and M. Fu: *Acta Mater.*, 2011, vol. 59, pp. 2412–22.
39. L. Kucherov and E.B. Tadmor: *Acta Mater.*, 2007, vol. 55, pp. 2065–74.
40. M.A. Meyers, O. Vöhringer, and V.A. Lubarda: *Acta Mater.*, 2001, vol. 49, pp. 4025–39.
41. L. Capolungo, P.E. Marshall, R.J. Mccabe, I.J. Beyerlein, and C.N. Tome: *Acta Mater.*, 2009, vol. 57, pp. 6047–56.

42. M.H. Yoo, J.R. Morris, K.M. Ho, and S.R. Agnew: *Metall. Mater. Trans. A*, 2002, vol. 33, pp. 813–22.
43. Z. Wu and W.A. Curtin: *Nature*, 2015, vol. 526, pp. 62–67.
44. F. Wang and S.R. Agnew: *Int. J. Plast.*, 2016, vol. 81, pp. 63–86.
45. I.J. Beyerlein, J. Wang, K. Kang, S.J. Zheng, and N.A. Mara: *Mater. Res. Lett.*, 2013, vol. 1, pp. 89–95.
46. J. Wang, Q. Zhou, S. Shao, and A. Misra: *Mater. Res. Lett.*, 2017, vol. 5, pp. 1–19.
47. M.R. Barnett, M.D. Nave, and A. Ghaderi: *Acta Mater.*, 2012, vol. 60, pp. 1433–43.
48. J. Tao, S. Hu, and L. Ji: *Mater. Charact.*, 2016, vol. 120, pp. 185–94.
49. T. Goswami: *Mater. Des.*, 2003, vol. 24, pp. 423–33.
50. B.P. Sanders, S. Mall, and R.B. Pittman: *Compos. Sci. Technol.*, 1999, vol. 59, pp. 583–91.
51. A.H. Noroozi, G. Glinka, and S. Lambert: *Int. J. Fatigue*, 2007, vol. 29, pp. 1616–33.
52. L. Lu, J. Li, C.Y. Su, P.Y. Sun, L. Chang, B.B. Zhou, and X.H. He: *Thero. Appl. Fract. Mech.*, 2019, vol. 100, pp. 215–24.
53. R. Pippan and A. Hohenwarter: *Fatigue Fract. Eng. Mater. Struct.*, 2017, vol. 40, pp. 471–95.
54. Z.J. Zhang, P. Zhang, L.L. Li, and Z.F. Zhang: *Acta Mater.*, 2012, vol. 60, pp. 3113–27.
55. W. Schaef and M. Marx: *Acta Mater.*, 2012, vol. 60, pp. 2425–36.